Chapter Four

The Damped Driven Easy-Plane Ferromagnet

4.1 Introduction

In this chapter the dynamics of the classical easy-plane ferromagnet under the influence of arbitrary driving fields is studied by numerical integration of the equations of motion on a discrete lattice. A phenomenological Landau-Gilbert damping term is included in the equations, effectively to limit the energy of the system, and to model processes in a real material that couple to the spin degrees of freedom and remove energy from them. The various configurations of DC plus AC driving fields will be seen to produce a range of possible spin motions. In some cases, all of the spins move together as a single unit, thereby making the exchange energy of the Hamiltonian constant. Then the system has the same dynamics as a single isolated spin (since no external "noise" is included in these simulations). In other cases, spatially periodic structures with periods less than the system size can be generated. In these cases the time behavior is also periodic, with some set of harmonics of the driving frequency present in the power spectrum. A small change of a parameter, however, such as the strength of the AC driving field, might cause the time behavior to become chaotic or space-time intermittent, indicated by a rapid growth in the noise level in the power spectrum between the original harmonics that were present. In this situation, the spatial structure may change from one that is in phase with the driving frequency to one that does not remain at any fixed phase to the driving, and undergoes gradual shape changes over each period of the driving field. Under some circumstances (to be described below) a further increase of the varied parameter induces a transition back to a spatially and temporally periodic motion.

Further increases, however, would be likely to re-initiate the chaotic behavior.

There are other examples of dissipative nonequilibrium nonlinear many degree-of-freedom systems which exhibit spatial pattern selection, as does this ferromagnet. Examples are convection cells (Cross 1982) and reaction-diffusion systems (Meinhardt 1982). In these systems strong mode-locking exists and a small number of (nonlinear) modes dominates the space-time evolution, both in chaotic (or intermittent) and quiescent paramter regimes. Thus we might expect that these many degree-of-freedom systems with strong spatial coupling may be adequately modeled by low-D maps, which have been studied thoroughly in recent years (see Physica 7D 1983). But more importantly for the present discussion, it should be emphasized that the phenomena of pattern formation, low-D chaos and co-existing coherence and chaos may be intimately related in these types of systems. For instance, the chaotic dynamics may develop through chaotic motions of the collective coordinates which identify the dominant patterns in the quiescent regime. Probably only a small loss of mode-locking is responsible for temporal chaos in the presence of spatial coherence. That is, only a small number of modes become unstable as some parameter is changed, the rest remaining strongly locked. By numerical simulations, we wish to provide evidence that the driven ferromagnetic chain falls into this class of systems, and that it may be an example where solid state chaos can be observed experimentally.

Various simple combinations of a single DC field component (such as $\hat{x}$) plus a single AC field component (such as $\hat{z}$) have been considered, ruling out rotating fields. In particular, this example field configuration mentioned reduces to the damped driven sG equation under the assumption of small out-of-plane spin tipping. Two types of initial conditions

have been used: 1) random fluctuations of the spin variables from some completely aligned configuration; 2) a symmetric breather initial profile, taken directly from the breather solution to the sG limit as in Chapter 2. These asymmetric and symmetric initial profiles were used to test whether the dynamics would force the motion into one with some symmetry predetermined by the equations of motion. In addition to this, the equations of motion for a single spin were also studied, in order to characterize the effect of spatial coupling between spins on the time dynamics of the multispin case.

The dynamics for a given field configuration has been characterized by various diagnostic methods. These include a) power spectra of the xyz spin components of arbitrarily chosen individual spins in the lattice, using a fast fourier transform, b) calculating graphs of $\langle \vec{M}(t) \rangle$, the spatial average of the magnetization vs. time, usually a good indicator of a chaotic power spectrum; c) phase plane plots, for example, of $\dot{S}_n^x$ vs. S_n^x plotted at specified time intervals; d) Poincare section plots, similar to the phase planes, but using data at integral multiples of the driving period; e) spatial spin profiles at various times, and also space-time plots of the dynamics of the spin variables; f) space or time correlation functions, such as $\langle S_n^{\alpha}(0) \; S_n^{\beta}(t) \rangle$; g) calculations of the Grassberger-procaccia (GP, 1983) "correlation dimension" for the dynamics. This last mentioned diagnostic tool gives an estimate of the number of modes strongly involved in the dynamics. It will be seen that generally, even when the evolution becomes chaotic, this dimension is a very small number ($\lesssim$ 2-3), indicating that the spatial coherence of the structures generated in the motion limits the number of degrees of freedom (i.e. normal modes, in some sense) involved. This effect generally has been referred to by Bishop (1984) as a competition between spatial coherence and temporal chaos. If

there were N noninteracting spins in the system, each with 2 degrees of freedom (3 spin components minus 1 constraint on spin length), then the chaotic dynamics would be expected to be described by a GP dimension of 2N. The formation of spatially coherent structures in the interacting spin system severely reduces this dimension to a much smaller number, usual not an integer.

A short explanation of the GP dimension is probably in order. The dimension is calculated from a sequence of p values of the output variable, say S^x, taken at m of the lattice sites. m is called the embedding dimension. These m x-components of the spins are used to form a vector $\vec{x}_i$, at the ith output time step, $t = i\Delta t$. The sequence of p vectors $\vec{x}_i$, where p is a number of the order of 10,000, is actually used to calculate the dimension. All possible pairs of $\vec{x}_i$ and $\vec{x}_j$ at different times are found that satisfy $|\vec{x}_i - \vec{x}_j| < r$. The number n(r) of pairs $(\vec{x}_i, \vec{x}_j)$ satisfying $|\vec{x}_i - \vec{x}_j| < r$ usually scales in a simple fashion with r, as $r \to 0$,

$$n(r) \sim r^{\nu} \quad . \tag{4-1}$$

The GP dimension ν can then be found from the slope of the logarithm of n(r) vs. the logarithm of r. For maximum computational speed the mod function is defined to be the largest component of the vector,

$$|\vec{x}| \equiv \max(x_1, x_2, x_3 \ldots x_m) \quad . \tag{4-2}$$

This dimension has also been called a "correlation dimension".

4.2 Equations of Motion with Damping

The undamped equations of motion for the easy-plane ferromagnet are given in equation (2-3). A phenomenological damping can be added in two slightly different ways, according to de Leeuw et al. (1980). Each

involves changing the definition of the effective torque in (2-3). The first was introduced by Landau and Lifshitz (LL), and changes the equations of motion to

$$\dot{\vec{S}}_n = \vec{S}_n \times \vec{G}_n \tag{4-3a}$$

$$\vec{G}_n = \vec{F}_n - \frac{\varepsilon}{S}(\vec{S}_n \times \vec{F}_n) \tag{4-3b}$$

$$\vec{F}_n = J(\vec{S}_{n-1} + \vec{S}_{n+1}) + g\mu_B\vec{B} - 2AS_n^z\hat{z} \quad . \tag{4-3c}$$

The parameter ε is a dimensionless damping constant, usually satisfying $\varepsilon \ll 1$. $\vec{F}_n$ is the same variable introduced in the undamped case. The second type of phenomenological damping was introduced by Gilbert and Kelly (GK), and involves using $\vec{G}_n$ re-defined by

$$\vec{G}_n = \vec{F}_n - \frac{\varepsilon}{S}(\dot{\vec{S}}_n) \quad , \tag{4-4}$$

with the dynamics satisfying (4-3a) and (4-3c). For very small ε, the two types of damping are equivalent. From the point of view of computer implementation of the equations in terms of xyz components, it is simplest to program the LL damping, since the time derivative appears on only one side of the equation. Therefore LL damping has been used in these numerical simulations. Nevertheless it is useful to consider the different forms of the equations of motion with the two types of damping, in terms of the spherical polar coordintes ϕ_n and θ_n, the in-plane and out-of-plane angles,

$$\vec{S}_n = S(\cos\theta_n \cos\phi_n,\ \cos\theta_n \sin\phi_n,\ \sin\theta_n) \quad . \tag{4-5}$$

After some algebra, the discrete equations of motion using GK damping are found to be

$$(1 + \varepsilon^2)\ \dot{\phi}_n \cos\theta_n = T_n^{\phi} + \varepsilon T_n^{\theta} \tag{6-4a}$$

$$(1 + \varepsilon^2)\ \dot{\theta}_n = T_n^{\theta} - \varepsilon T_n^{\phi} \quad , \tag{6-4b}$$

where the torque components T_n^{ϕ} and T_n^{θ} are

$$T_n^{\phi} = JS\{\sin\theta_n[(\cos\theta_{n-1}\cos(\phi_{n-1} - \phi_n) + \cos\theta_{n+1}\cos(\phi_{n+1} - \phi_n)]$$

$$- \cos\theta_n(\sin\theta_{n-1} + \sin\theta_{n+1})\}$$

$$+ g\mu_B\{\sin\theta_n\ (B_x\cos\phi_n + B_y\sin\phi_n) - B_z\cos\theta_n\} + 2AS\sin\theta_n\cos\theta_n \tag{4-7a}$$

$$T_n^{\theta} = JS[\cos\theta_{n-1}\sin(\phi_{n-1} - \phi_n) + \cos\theta_{n+1}\sin(\phi_{n+1} - \phi_n)]$$

$$+ g\mu_B(B_y\cos\phi_n - B_x\sin\phi_n) \quad . \tag{4-7b}$$

In the case of only an x-component to the applied field, these have already been given in the right hand side of equation (2-5). One finds that the similar equations for LL damping are taken from equations (4-6) by retaining only the first order terms in ε,

$$\dot{\phi}_n \cos\theta_n = T_n^{\phi} + \varepsilon T_n^{\theta} \tag{4.8a}$$

$$\dot{\theta}_n = T_n^{\theta} - \varepsilon T_n^{\phi} \quad . \tag{4-8b}$$

Therefore, there should be no real distinction between the dynamics using the two different forms of damping. Only a rescaling of the time variable is necessary to relate the two. Equations which follow will be written for LL damping; the equations for GK damping are obtained from these by changing $t \rightarrow t/(1+\varepsilon^2)$.

Taking the continuum limit, n is replaced by position z. Rescaling the time and space variables as in Chapter 2, and the field,

$$t' = (2AS/\hbar)t \tag{4-9a}$$

$$\xi^2 = (2A/Ja^2)z^2 \tag{4-9b}$$

$$\vec{b} = g\mu_B\vec{B}/JS \quad , \tag{4-9c}$$

the continuum limit torque components are

$$T^{\phi}(\xi) = -\theta_{\xi\xi} + (1-\phi_{\xi}^2)\sin\theta\cos\theta + \sin\theta(b_x\cos\phi + b_y\sin\phi) - b_z\cos\theta \tag{4-10a}$$

$$T^{\theta}(\xi) = \phi_{\xi\xi\xi}\cos\theta - 2\phi_{\xi}\theta_{\xi}\sin\theta + b_y\cos\phi - b_x\sin\phi \quad . \tag{4-10b}$$

Equations (4-10), taken together with the continuum version of (4-8) with t' replacing t give the continuum equations of motion for arbitrary driving fields. Next, the field configuration leading to a damped driven sG equation is considered.

4.3 Damped Driven Sine-Gordon Limit

As for the sG limit obtained in Chapter 2, the sG limit is obtained here by first assuming strong easy-plane anisotropy that limits the spins to only small out-of-plane motions $\theta \ll 1$. In addition to this, there is a DC field in the easy plane, B_x, together with an AC field in the z direction, perpendicular to the easy plane, which has a tendency to apply a torque that drives changes in the in-plane angle ϕ. Linearizing in θ, the dynamics is approximately described by

$$\phi_{t'} = \theta - b_z + \varepsilon(\phi_{\xi\xi\xi} - b_x\sin\phi) \tag{4-11a}$$

$$\theta_{t'} = \phi_{\xi\xi} - b_x \sin - \varepsilon(\theta - b_z) \quad . \tag{4-11b}$$

The variable θ can be eliminated, leading to

$$\phi_{t't'} = (1+\varepsilon^2)(\phi_{\xi\xi} - b_x \sin\phi) - \frac{\partial b_z}{\partial t'} + \varepsilon[\phi_{\xi\xi t'} - (1 + b_x \cos\phi)\phi_{t'}] \quad , \tag{4-12a}$$

and assuming $\varepsilon \ll 1$, the corresponding solution for θ is

$$\theta \simeq \phi_{t'} + b_z \tag{4-12b}$$

Equation (4-12a) is the damped driven sG equation. It includes two types of damping. However, the $\phi_{\xi\xi t'}$ term is generally smaller than the $\phi_{t'}$ term, so it can be dropped. By once more rescaling the space and time variables, (4-12a) can be compared to the dimensionless damped driven sG equation, in the notation of Bishop et al. (1983),

$$\phi_{xx} - \phi_{\tau\tau} = \sin\phi + \alpha\phi_{\tau} + \gamma(\tau) \quad . \tag{4-13}$$

Equations (4-12a) and (4-13) are equivalent if we take

$$x = b_x^{1/2}\xi \tag{4-14a}$$

$$\tau = [g\mu_B B_x 2AS(1 + \varepsilon^2)]^{1/2} t \tag{4-14b}$$

$$\alpha = \frac{\varepsilon}{\sqrt{b_x(1+\varepsilon^2)}} (1 + b_x \cos\phi) \tag{4-15a}$$

$$\gamma(\tau) = \frac{1}{\sqrt{b_x(1+\varepsilon^2)}} \frac{\partial b_z}{\partial \tau} \quad . \tag{4-15b}$$

The effective driving of the sG equation is proportional to the time derivative of the z-component of the magnetic field. The dimensionless

damping constant α is seen to have a slight dependence on ϕ, but usually $b_x \ll 1$ will be assumed so that this is not important.

The simplest type of driving to consider is a sinusoidal time dependent field,

$$\gamma(\tau) = \Gamma \sin\omega_d\tau = \Gamma \sin\omega t \quad , \tag{4-16}$$

which is obtained from

$$B_z(t) = -B_{0z} \cos\omega t \quad . \tag{4-17}$$

The dimensionless sG driving strength is related to the amplitude B_{0z} and frequency ω fo the AC field by

$$\Gamma = \frac{\omega}{2AS(1+\varepsilon^2)} \frac{B_{0z}}{Bx} \quad . \tag{4-18}$$

From a physical point of view, it is helpful to define a driving frequency measured in kilogauss, ω_{kG}, as the applied field strength would be, by

$$g\mu_B\omega_{kG} \equiv \omega \quad , \tag{4-19}$$

or

$$b_d \equiv \frac{g\mu_B\omega_{kG}}{2AS} \quad . \tag{4-20}$$

Then the dimensionless driving strength, in the limit $\varepsilon \to 0$, can be expressed by the simple relation

$$\Gamma = b_d \frac{B_{0z}}{bx} \quad . \tag{4-21}$$

All three "field strengths" are normalized to the anisotropy constant. Also note that the sG dimensionless driving frequency ω_d is

$$\omega = \frac{\omega}{\sqrt{g\mu_B B_x 2AS(1+\varepsilon^2)}} = \frac{b_d}{\sqrt{b_x(1+\varepsilon^2)}} \tag{4-22}$$

As an example application of the formulae, for the $CsNiF_3$ anisotropy A = 4.5 K, taking $\varepsilon = 0.1$, $B_x = 5$ kG, $B_{0z} = 30$ kG gives $\Gamma = 0.8$, $\alpha = 0.33$, using $\cos\phi = 0$ in the expression for α. This is very close to a point at which there is a transition to chaos in the sG equation, and one would expect the same to be true in the ferromagnet using the full equations of motion. Results are given below that show this to be the case.

4.4 Numerical Simulation

The equations of motion in terms of xyz spin components, on a discrete lattice, equation (4-3), were integrated numerically using a 4th order Adams-Bashforth-Moulton predictor-corrector method with a fixed time step of 0.02 (using time units of $\hbar/JS$). This integration scheme is a standard method; it is outlined in Appendix A. A fixed time step method was used to simplify the collection of data for power spectra and other diagnostics. Simulations were carried out both for an individual spin, and for N = 150 spins, satisfying periodic boundary conditions.

Five field configurations were studied, including the sG case. They are

1) $\vec{B} = B_{AC}\,\hat{z}$, perpendicular to the easy plane;
2) $\vec{B} = B_{AC}\,\hat{x}$, within the easy plane;
3) $\vec{B} = B_{DC}\,\hat{x} + B_{AC}\,\hat{z}$, the sG limit case;
4) $\vec{B} = B_{DC}\,\hat{x} + B_{AC}\,\hat{x}$, parallel AC plus DC in the easy plane;
5) $\vec{B} = B_{DC}\hat{x} + B_{AC}\hat{y}$, perpendicular AC plus DC in the easy plane.

A symmetric initial condition for the N spin case was taken to be the stationary (zero velocity) breather solution to the dimensionless sG equation,

$$\phi = 4 \tan^{-1} \frac{\sqrt{1-\omega_B^2}}{\omega_B} \frac{\sin \omega_B(\tau-\tau_0)}{\cosh(\sqrt{1-\omega_B^2}x)} \tag{4-23a}$$

$$\theta = \phi_\tau \quad . \tag{4-23b}$$

This generally has the appearance of a bound $K\bar{K}$ pair, with an internal oscillation frequency ω_B, if the dynamics were to evolve according to the sG equation.

The following algorithm was used to generate the random initial conditions. First, all spins were set parallel to some direction, for instance, the x-axis. Then a vector $\ell\hat{u}_n$ of length ℓ was added to each of the spin vectors, where ℓ was a random number somewhere between zero and L, and the unit vectors $\hat{u}_n$ were chosen in random directions with uniform probability over the unit sphere. The sum vectors at each site, $\hat{x} + \ell\hat{u}_n$, was then renormalized back to unit length, and this was then the initial condition. Obviously the parameter L determines the degree of randomness in this initial configuration. As $L \to \infty$, the initial configuration becomes one where the spins are uniformly distributed over the unit sphere. As $L \to 0$, the initial state is only a small random fluctuation from the perfectly aligned set of spins.

Most of these simulations were done using $CsNiF_3$ parameters, A/J = 0.19, g = 2.4 and the phenomenological damping constant $\varepsilon = 0.1$. Driving field strengths ranged from zero to 30 kG or more. Two driving field frequencies were used; $\omega_{kG} = 2.5$ kG and $\omega_{kG} = 7.5$ kG, corresponding to real frequencies of 8.4 GHz and 25 GHz respectively. Results for single

spin simulations are given in the next section, followed by the results for the 150 spin simulations.

4.5 Single Spin Results

The simulations using ω_{kG} = 2.5 kG showed only periodic behavior up to fields of the order of 30 kG, so a higher frequency was tried. Using ω_{kG} = 7.5 kG proved to be much more interesting -- all results shown here are for that frequency, corresponding to ω = 0.05144 in these time units, or a period of 122 time units.

An overview of those results is shown in Figure 4.1. For these single spin simulations the spin was initially set on the x or y axis. These results are further summarized here as follows:

1) $\vec{B} = B_{AC}\,\hat{z}$; for driving amplitudes B_{AC} up to 30 kG only periodic motions result.

2) $\vec{B} = B_{AC}\,\hat{x}$, with

   B_{AC} = 2 - 4 kG, periodic motions at the driving frequency,

   B_{AC} = 5 kG, chaotic motion, see Figure 4.2,

   B_{AC} = 6.0, 8.0, 9.0 kG, period 3, period 1, period 2 motions respectively (see Figure 4.3), as indicated by the fundamental frequency in the power spectrum being a subharmonic of the driving frequency,

   B_{AC} = 10 - 30 kG, chaotic motions.

3) $\vec{B} = B_{DC}\,\hat{x} + B_{AC}\,\hat{z}$, with B_{DC} = 5.0 kG and

   B_{AC} = 2 - 33 kG , all periodic motions,

   B_{AC} = 34 - 60 kG, chaotic motion.

4) $\vec{B} = B_{DC}\,\hat{x} + B_{AC}\,\hat{x}$, with B_{DC} = 5.0 kG, gives an interesting set of period 1 to period 2 transitions,

   B_{AC} = 2 - 9 kG , period 1,

Figure 4.1 Overview of the time behavior for the single spin motion, for the five field configurations shown. The distinction between periodic and chaotic time behavior was made on the basis of the lack or presence of excess noise in the power spectrum between the harmonics of the driving frequency. See the text for further details in the various field regimes.

RESULTS FOR A SINGLE SPIN

$\vec{B}(t)=\vec{B}_{DC}+\vec{B}_{AC}\sin\omega t$

$\vec{B}_{DC}=0$

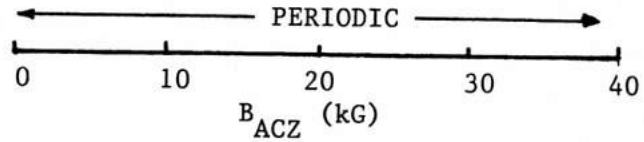

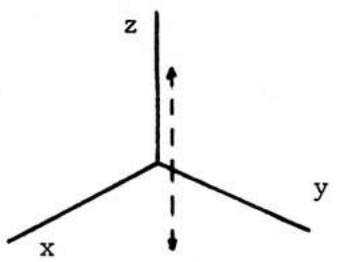

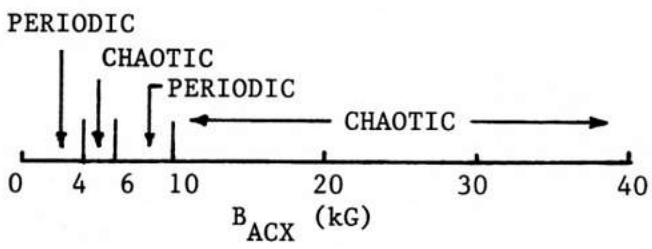

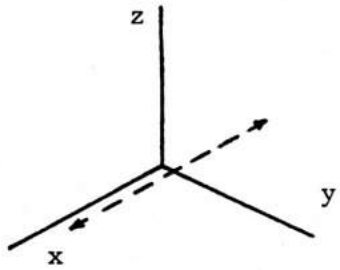

$B_{DCX}=5.0$ kG

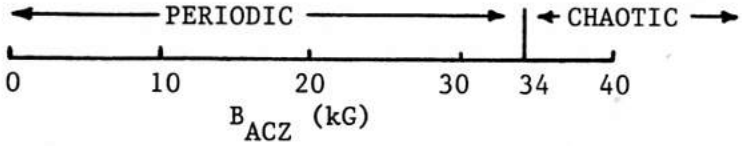

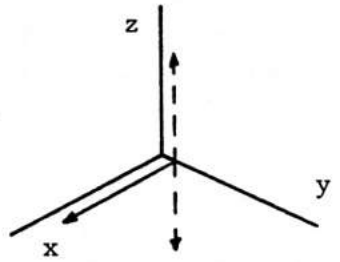

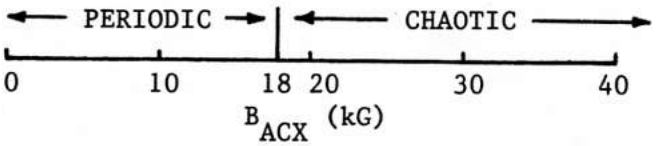

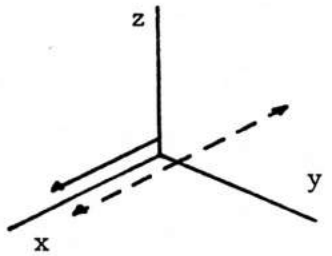

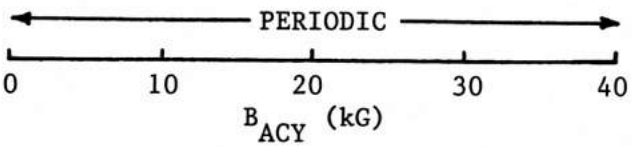

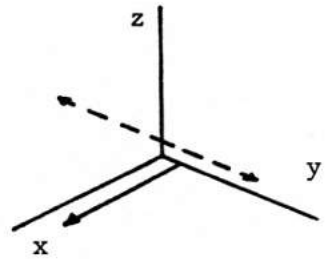

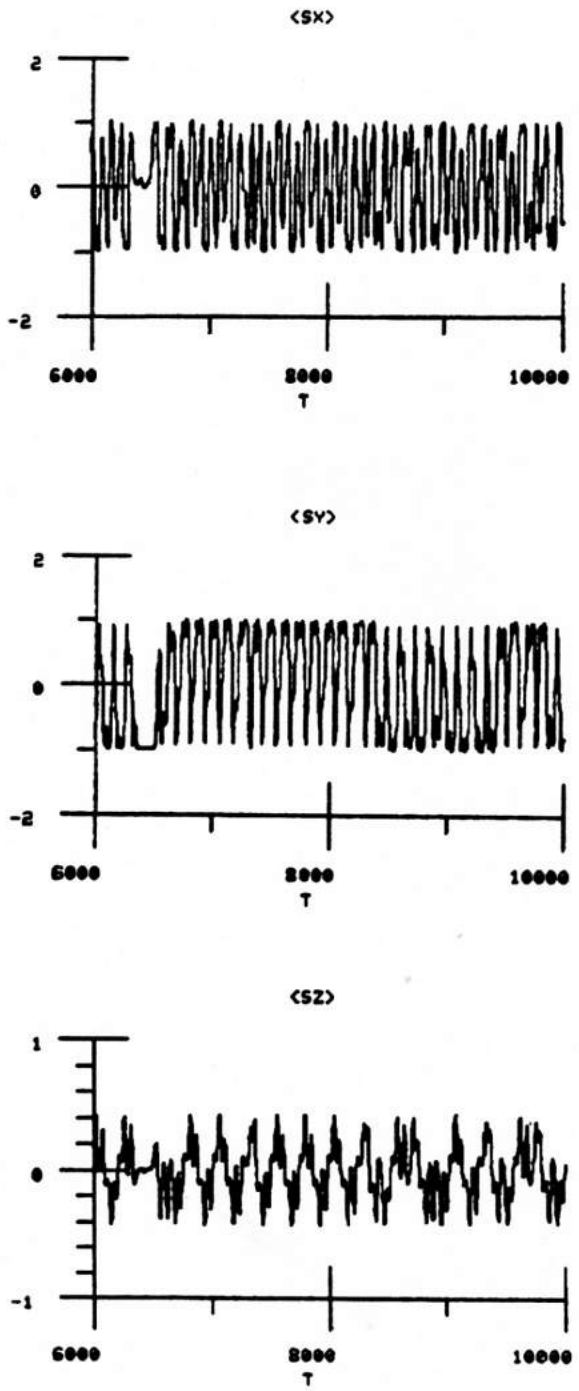

Figure 4.2a Chaotic motion of a single spin for $\vec{B}$ = 5.0 sinωt $\hat{x}$ kG, as seen in the xyz spin components vs. time, after an initial interval to allow transients to pass.

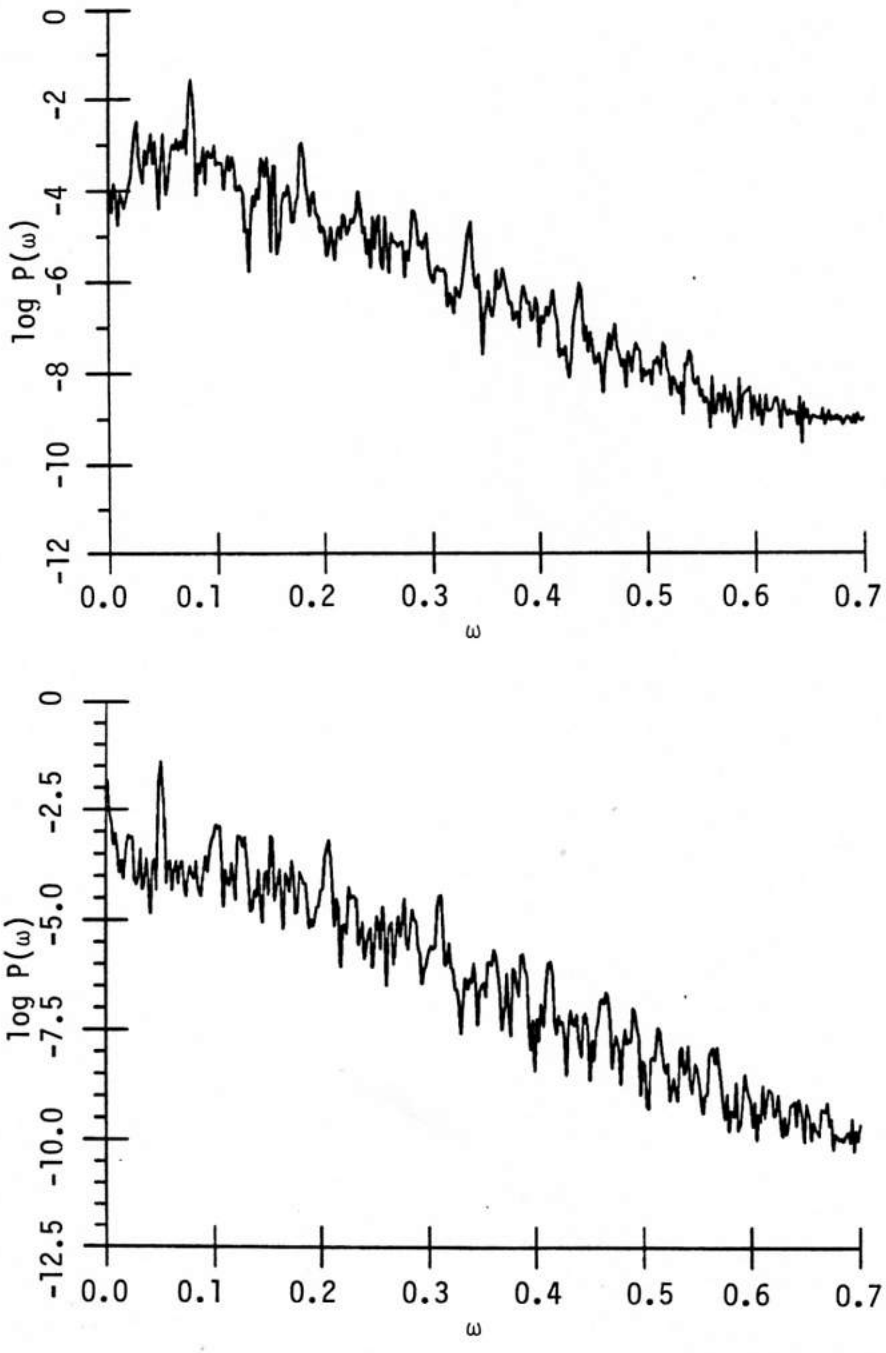

Figure 4.2b The chaotic power spectra (log scale) of the S^x(a) and S^y(b) spin motions from 4.2a. The driving frequency in these units is ω_d = .05144. Harmonics and subharmonics of this frequency are seen, together with considerable background between the peaks. Compare with the periodic power spectra in Figure 4.3.

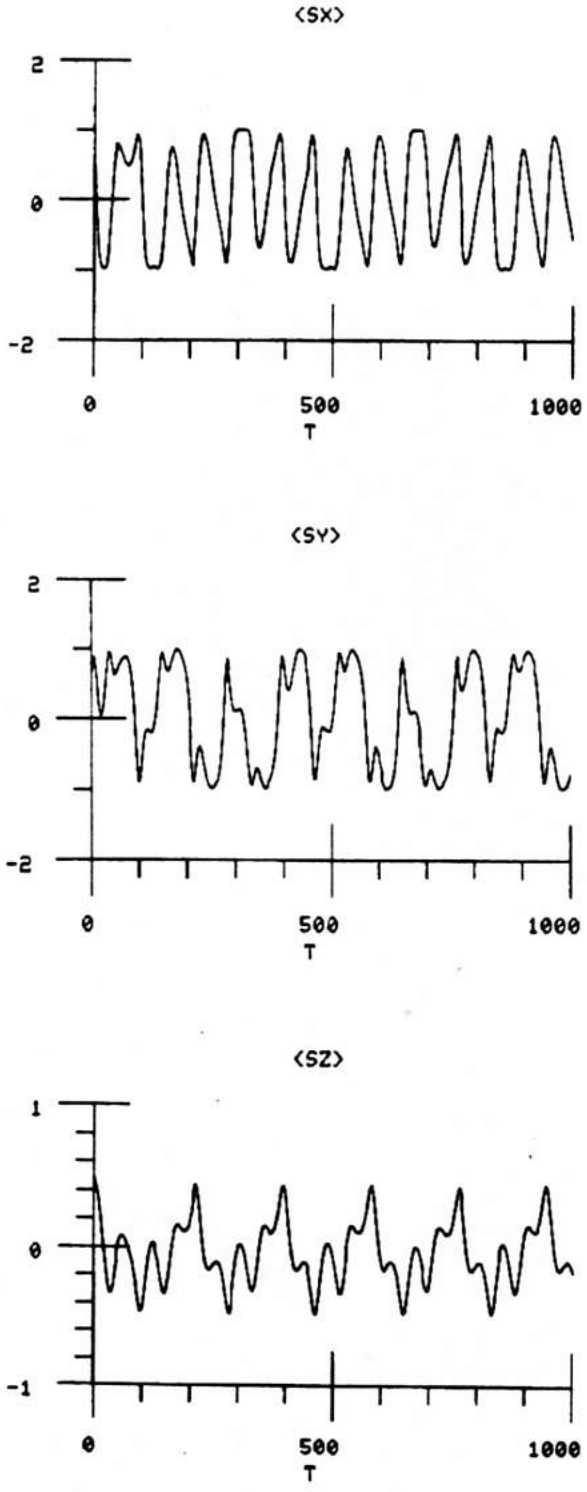

Figure 4.3a Period 3 motion for a single spin for $\vec{B}$ = 6.0 sinωt $\hat{x}$ kG. The driving period is approximately 130 time units, while the period of the S^x motion is 3 times this.

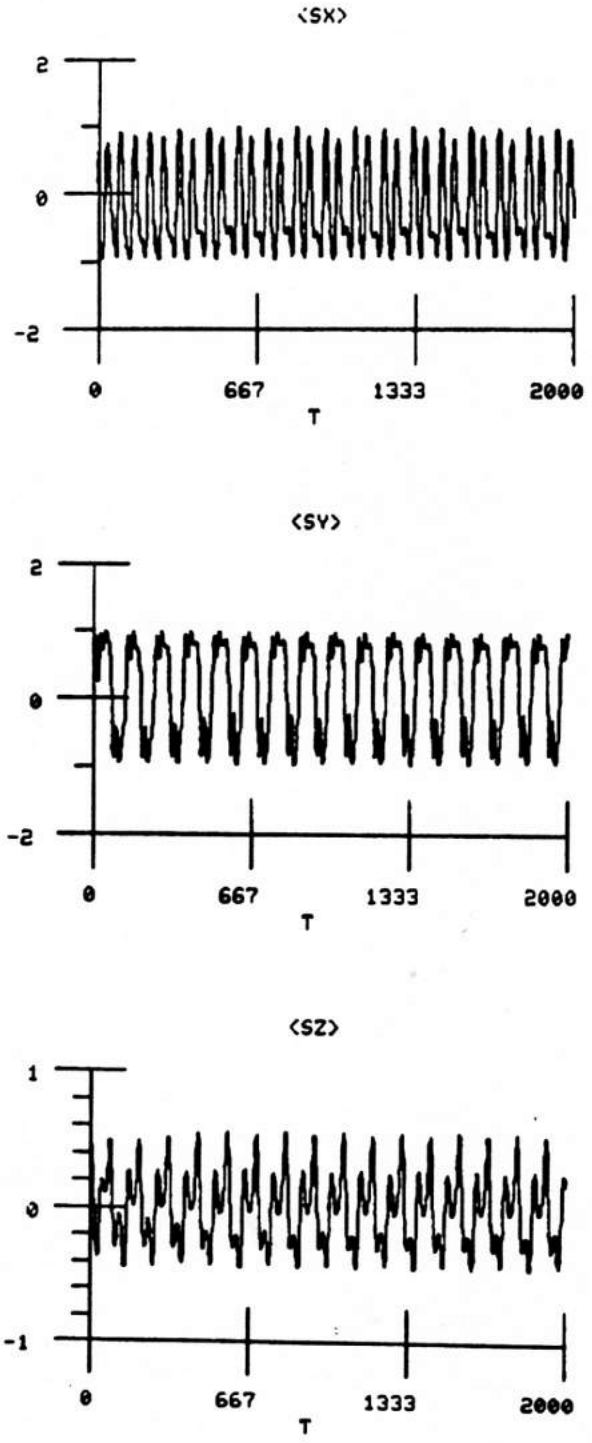

Figure 4.3 b Period 2 motion for a single spin for $\vec{B}$ = 9.0 sinωt $\hat{x}$ kG. There is only a small subharmonic component, as evidenced by the alternating peak heights in S^x and S^z.

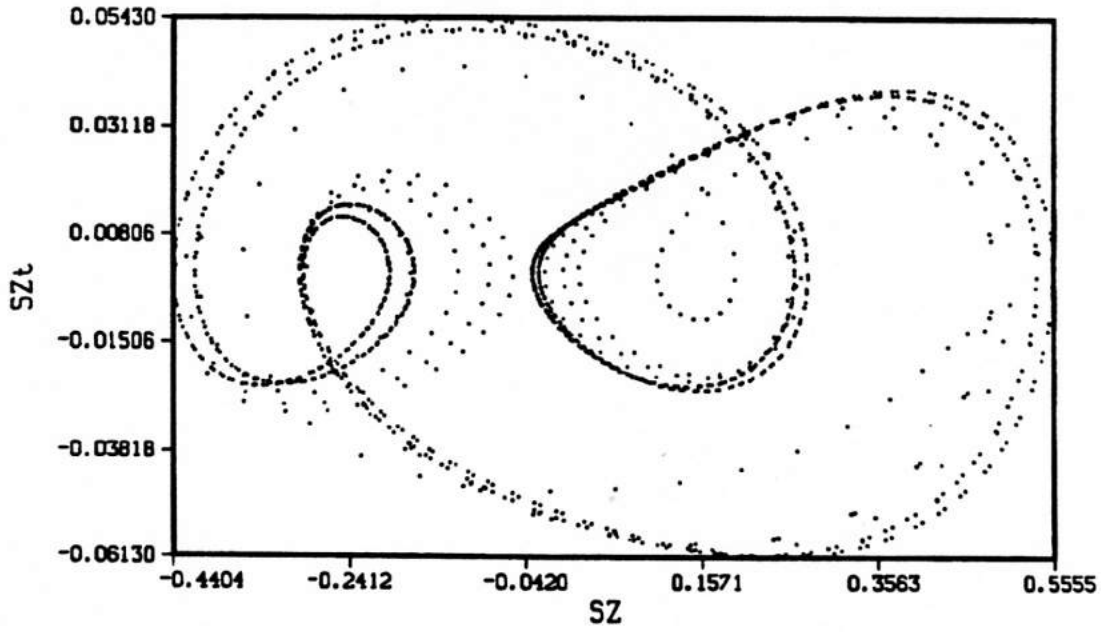

Figure 4.3c S^z phase plane plot for the period 2 motion of 4.3b. There is an initial transient, followed by motion along two curves.

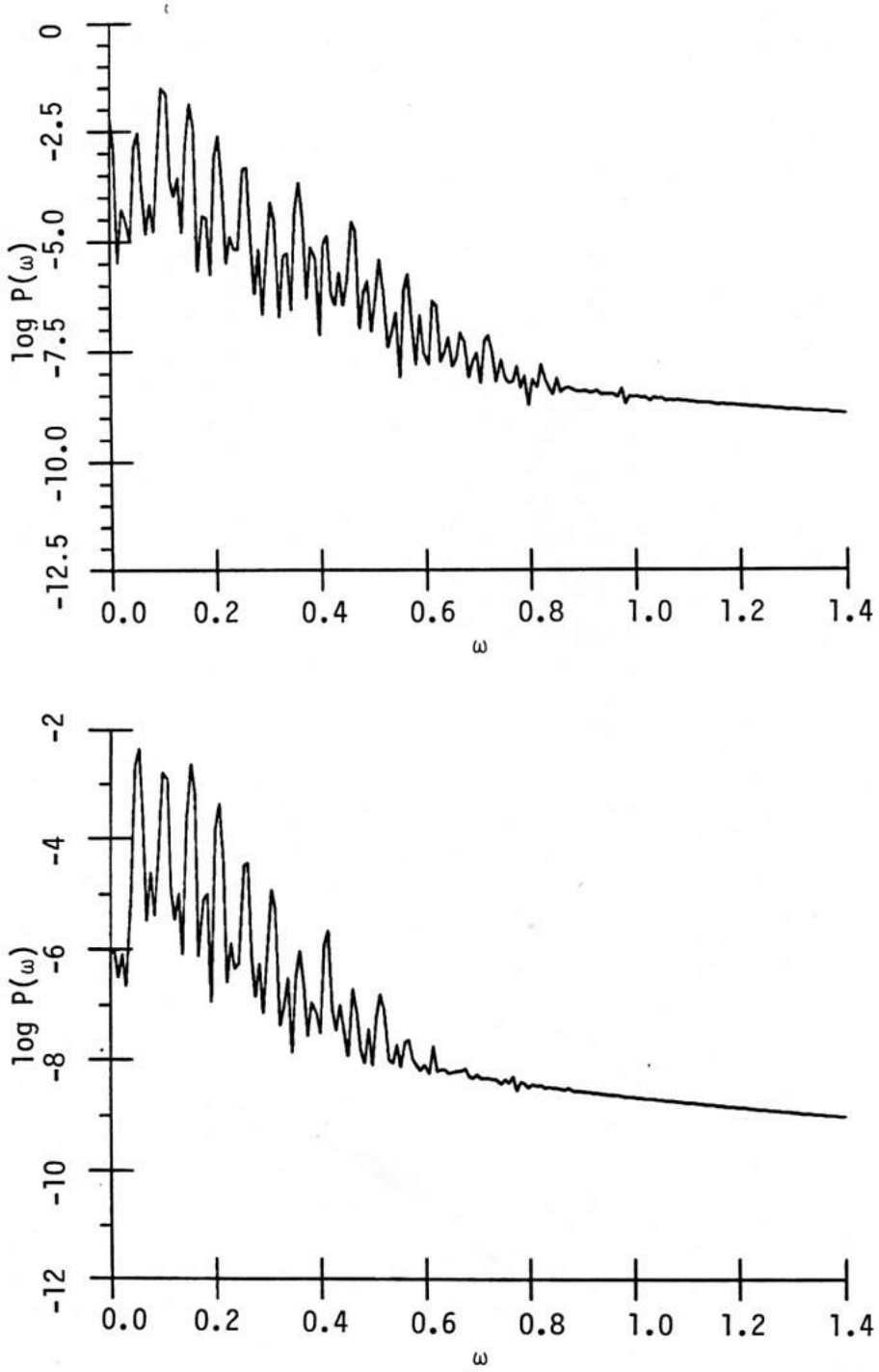

Figure 4.3d Power spectra (log scale) of the S^x(a) and S^z(b) motions from 4.3b. The subharmonic is small but clearly visible below the fundamental driving frequency ω_d = 0.05144.

B_{AC} = 9.5 - 15.0 kG , period 2,

B_{AC} = 16.0 kG , period 1,

B_{AC} = 17.0 kG , period 2,

B_{AC} = 18 - 30 kG , chaotic.

5) $\vec{B} = B_{DC}\,\hat{x} + B_{AC}\,\hat{y}$, with B_{DC} = 5.0 kG, gives all simply periodic motions for B_{AC} from 2 to 30 kG.

Cases 1 and 5 above did not produce any interesting time structures for the field strengths tried, but his does not rule out more interesting behavior at higher fields or frequencies. Cases 2, 3 and 4 all were capable of producing transitions to chaotic time behavior for fields below 35 kG; the sG limit case required the largest field strength for this to occur, while the case of only an AC field in the easy plane seems to be the easiest way to induce chaos. This latter case also has an interesting chaotic window between two periodic regimes.

4.6 Multispin Results: N = 150

On the basis of these results for the single spin motion, only field configurations 2, 3 and 4 were used for the 150-spin simulations, again at ω_{kG} = 7.5 kG. An overview of those results is given in Figure 4.4. Both symmetric and random initial conditions were used, however, the general time behavior was broadly independent of the type of initial condition, i.e., coexisting attractors were not prevalent. Somewhat more complicated spatial behavior was possible from the random initial conditions, since the symmetric breather initial conditions restricted the evolving structure to be symmetric. The following further comments can be made for the dynamics found in these field configurations

Figure 4.4 Overview of the time and space behavior for the motion of 150 spins with periodic boundary conditions, for the three field configurations shown. Comments above the axes refer to the time behavior, while comments below the axes refer to the spatial behavior. See the text for further details of the motion in the various field regimes.

RESULTS FOR 150 SPINS

$\vec{B}(t) = \vec{B}_{DC} + \vec{B}_{AC} \sin \omega t$

$\vec{B}_{DC} = 0$

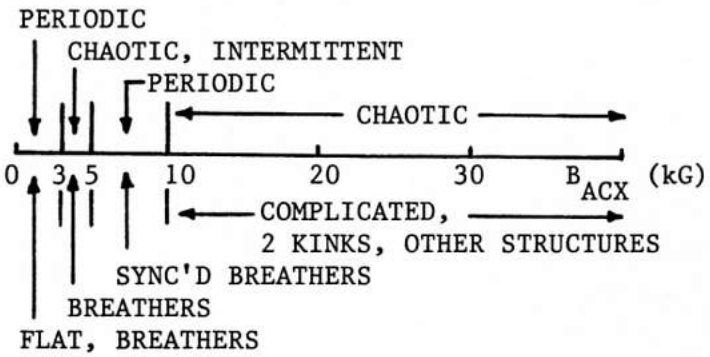

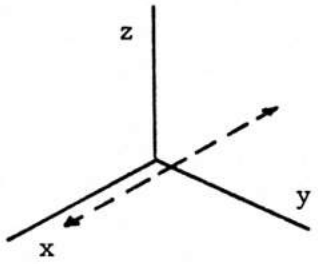

$B_{DCX} = 5.0$ kG

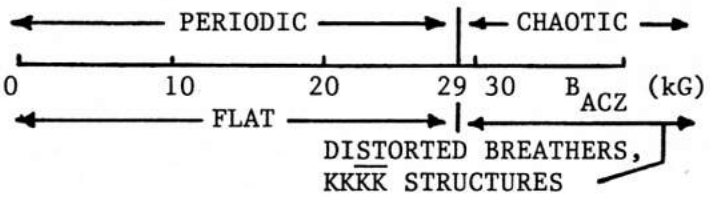

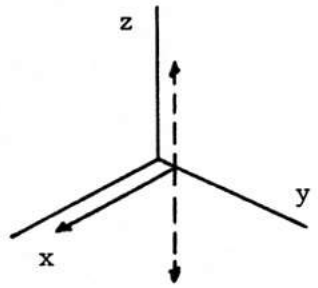

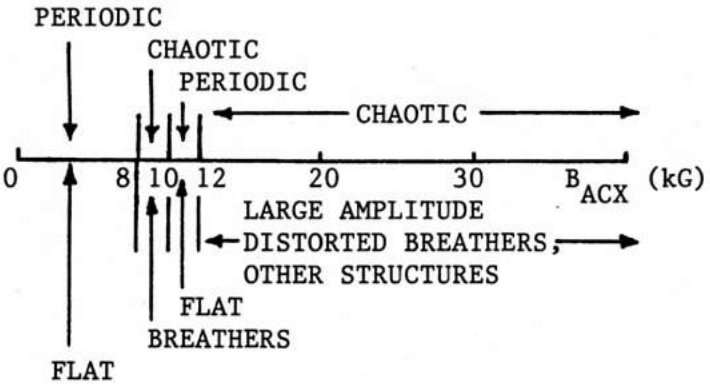

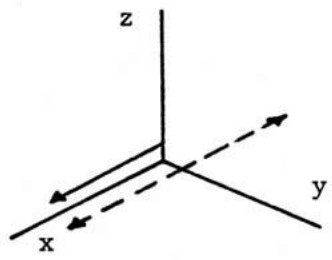

2) $\vec{B} = B_{AC}\,\hat{x}$

B_{ac} (kG)	Time Structure	Space Structure
2.0	period 1	flat, i.e. all spins parallel
3.0	period 1	single "breather"
4.0	intermittent, i.e., chaotic with periodic bursts, $\nu \sim 1.4$	when chaotic, 2 breathers, when periodic, nearly flat
5.0	period 2	period $\frac{1}{2}$, 2 breathers
6.0	period 2	bounding $K\bar{K}$ pair locked with the driving frequency
8.0	period 1	period $\frac{1}{2}$ locked with driving frequency
10.0	chaotic, possibly intermittent, $\nu \sim 1.5$	complicated period 1 structure
12-24	chaotic	complicated period 1 structures.

The parameter ν mentioned in the intermittent cases is the GP dimension. As for the single spin case, there is a chaotic regime between two periodic regimes, at approximately the same field strength as for the single spin. In both the single spin and multispin cases, there is a transition to chaos at 10.0 kG.

3) $\vec{B} = B_{DC}\,\hat{x} + B_{AC}\,\hat{z}$, with $B_{DC} = 5.0$ kG

B_{ac} (kG)	Time Structure	Space Structure
2-29	period 1	flat
30-60	chaotic, $\nu \sim 2.1$ at 35 kG	complicated period 1.

As for the single spin case, the sG limit does not have as much rich structure as configurations 2 and 4. Note that the transition to chaos for the multispin sG case is at a slightly lower field than in the single spin case.

4) $\vec{B} = B_{DC}\,\hat{x} + B_{AC}\,\hat{x}$, with $B_{DC} = 5.0$ kG,

B_{AC}(kG)	Time Structure	Space Structure
8.0	period 2	flat
9.0	chaotic	single breather
10.0	period 2	flat
11.0	chaotic	two kinks, or almost flat
12.0	chaotic	single K, or $K\bar{K}$
13-24	chaotic	single K, distorted breathers, other complicated structures.

Here there is additional structure that was not present in the single spin motion for $B_{AC} = 9.0$ kG -- a chaotic window. A careful search in the single spin simulations found only period 2 behavior there. Note that again the final transition to chaos at $\simeq$ 11 kG, is at much lower field strengh than for the single spin, where it was at 18 kG.

4.7 Examples of Low-D Chaos and Spatial Pattern Formation

Example One

The driving field configuration with only an AC field in the easy plane produced a number of transitions between periodic and chaotic time evolution, with associated drastic changes in the spatial structure, as the strength of the applied field was increased. On such example occurs for $4.0 < B_{ACX} < 5.0$ kG. At $B_{ACX} = 4.0$ sG, there is generally chaotic time evolution intermittently broken up by intervals of approximately periodic evolution. This is evident in Figure 4.6a, where the xyz components of the magnetization $\langle\vec{S}\rangle$ vs. time are shown starting from a random initial condition, shown in Figure 4.5. During the intervals where the motion is approximately periodic, one finds that the spatial structure is a smooth low amplitude wave. During the chaotic intervals, the spatial

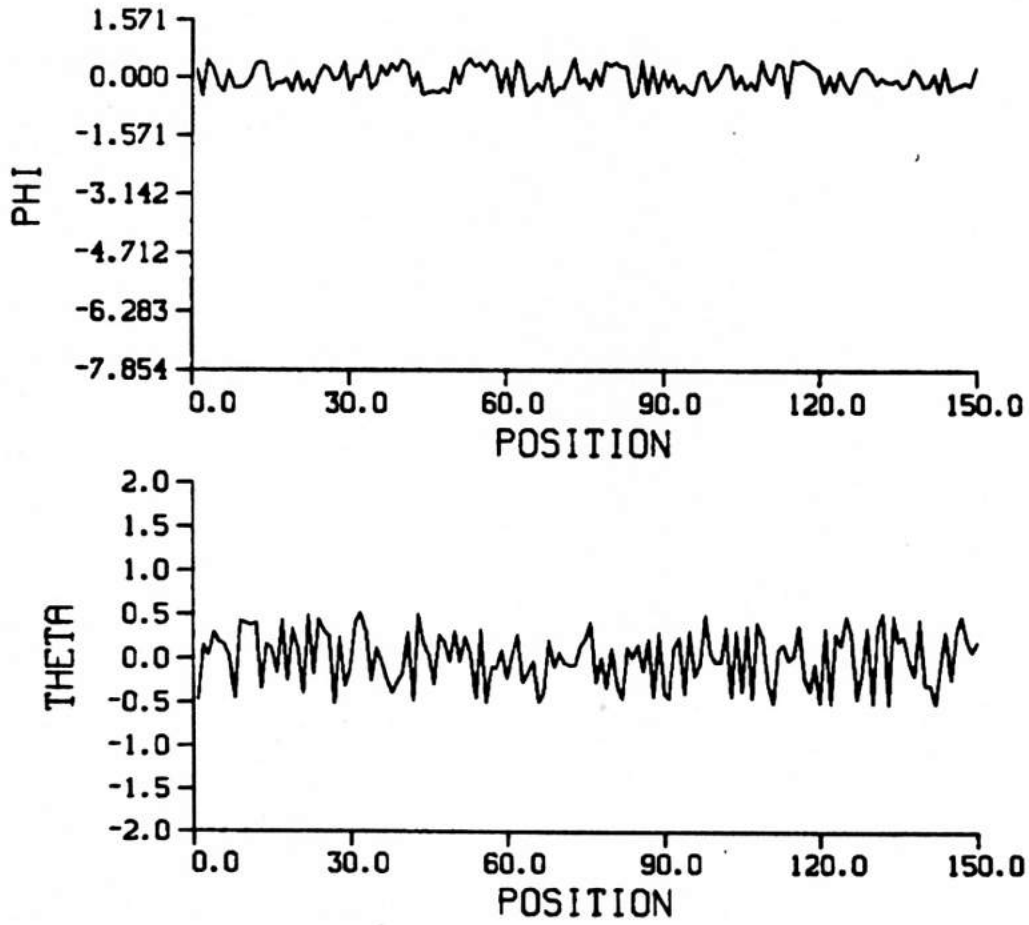

Figure 4.5 A typical random initial condition, in terms of the in-plane and out-of-plane angles ϕ and θ, for the parameter L = 0.5. Initially the spins were aligned with the x-axis, and given perturbations with lengths ranging from zero to L, in randomly chosen directions.

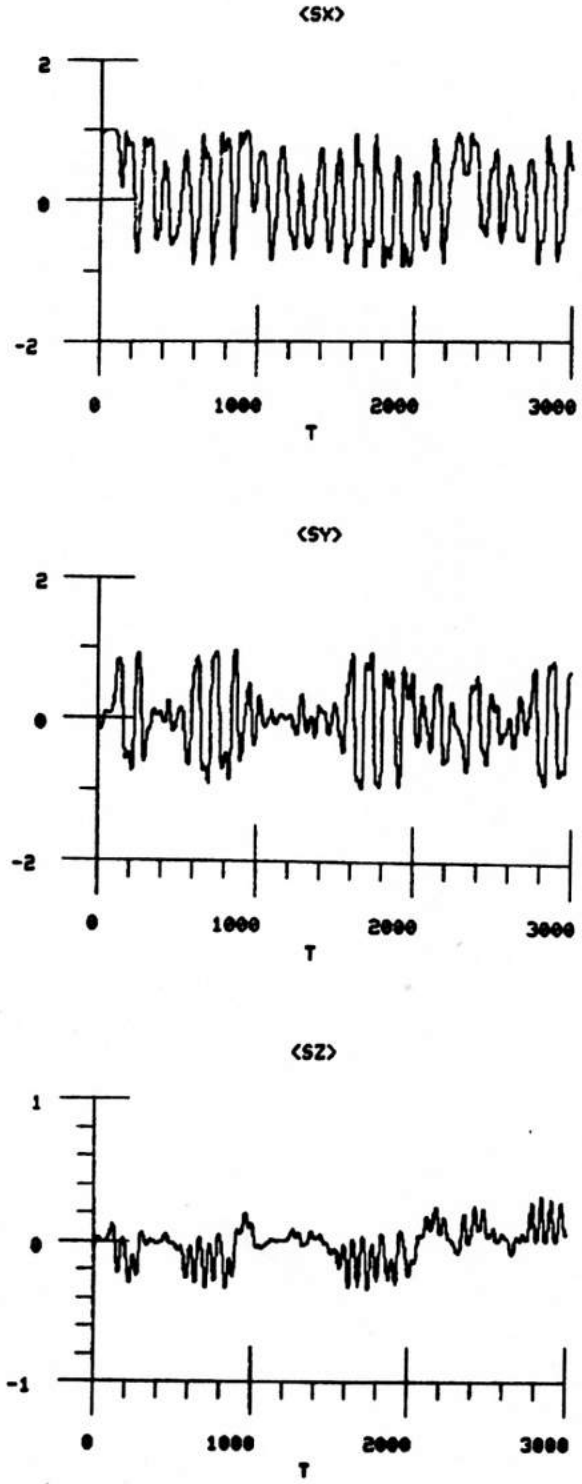

Figure 4.6a xyz components of $\langle \vec{S}(t) \rangle$ for B_{ACX} = 4.0 kG, starting from a random initial condition shown in Figure 4.5. There are approximately periodic intervals alternating with chaotic intervals.

structure appears to be two distorted breather-like modes. A space-time profile is shown in Figure 4.6b, where a transition from a periodic interval at t = 3000.0 to a chaotic interval can be seen.

Similar intermittent behavior can be obtained starting from the symmetric breather initial conditions, shown in Figure 4.7. Of course, since there is no asymmetry present in the system, the profile must remain symmetric as it evolves. A profile at t = 3000 is shown in Figure 4.8a, and the (chaotic) power spectra of the x and z components of the spin at the center of the chain are shown in Figure 4.8b.

The chaotic behavior at B_{ACX} = 4.0 kG can be contrasted with the periodic behavior at B_{ACX} = 5.0 kG. Starting from a random initial condition, the time evolution became simply periodic (period 1), as seen in $\langle \vec{S}(t) \rangle$, Figure 4.9a. The corresponding spacetime structure is shown in Figure 4.9b. The solution is obviously periodic in time and space -- the spatial period is half of the system length. Again similar behavior results from the symmetric breather initial condition, although now the period of the motion is twice the driver period. The power spectra of the x and z components of the spin at the center of the chain starting from symmetric breather initial conditions, are shown in Figure 4.10a. The magnetization vs. time is shown in Fig. 4.10b. Both of these demonstrate that the time behavior is period 2.

Example Two

The transition to chaos in the sG limit field configuration is the next example. Here we have B_{DCX} = 5.0 kG, consider the simply periodic case B_{ACZ} = 29.0 kG and compare it with the chaos for B_{ACZ} = 35.0 kG. For the lower field, and breather initial conditions, the spatial profile becomes flat -- all the spins move together. In Figure 4.11a we plot the profile as seen at t = 3000, and also the phase plane for the x-component

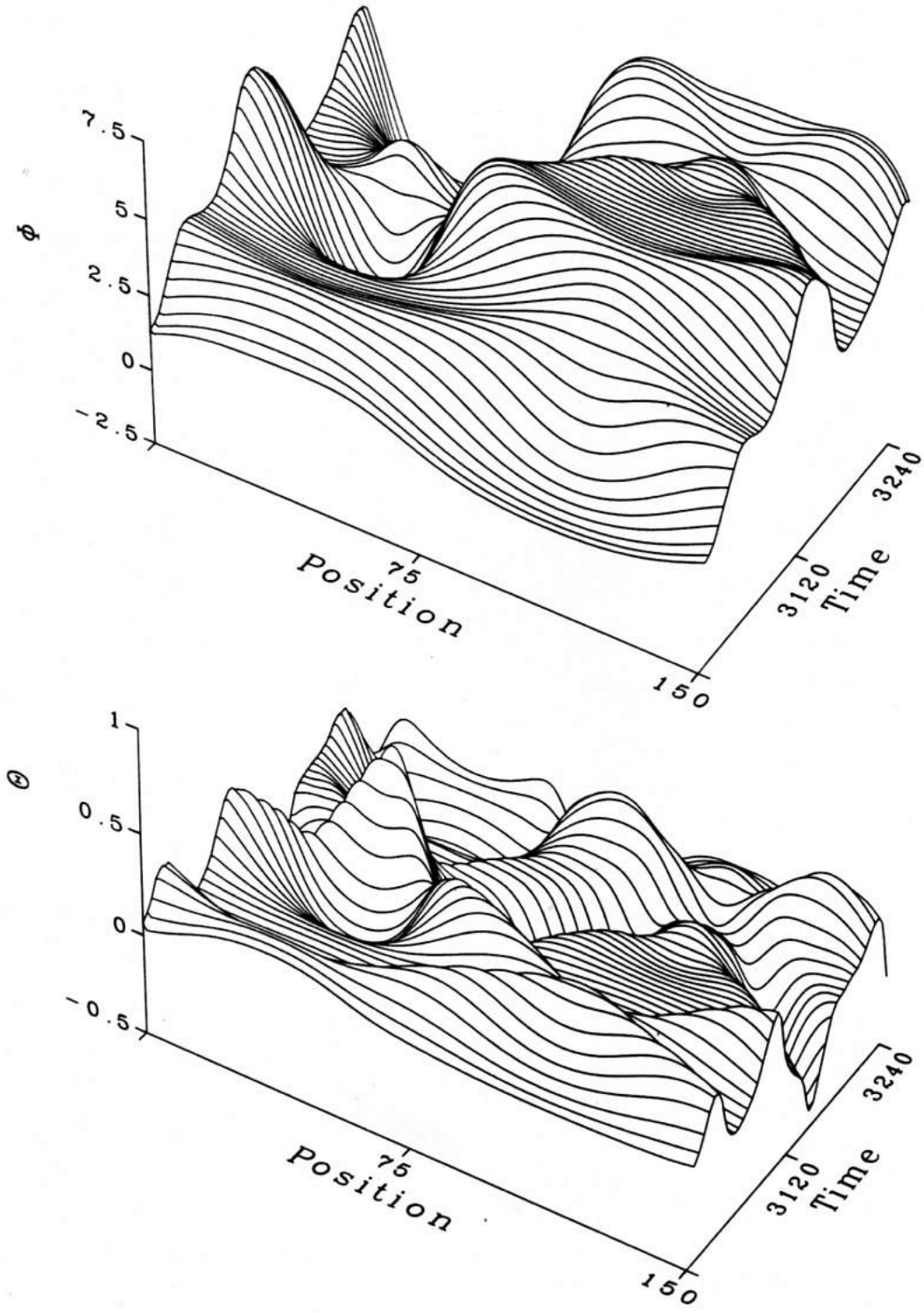

Figure 4.6b Space-time profiles of the in-plane and out-of-plane angles ϕ and θ for B_{ACX} = 4.0 kG, starting from a random initial condition at t = 0. There is a transition here from a smooth slowly varying low amplitude wave to a more complicated breather-like structure. The smooth spatial behavior is correlated with periodic time development while the complex spatial behavior is correlated with chaotic time development.

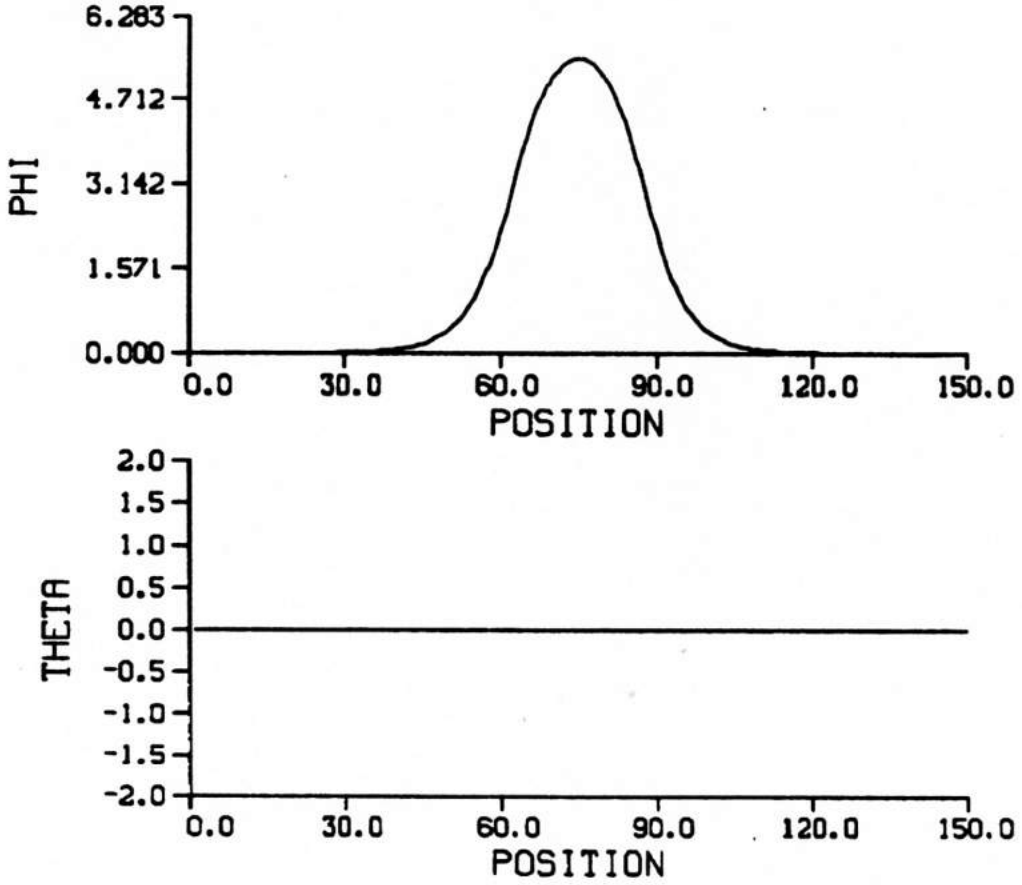

Figure 4.7 A symmetric breather initial condition with $\omega_B = 0.2$, equation (4-23).

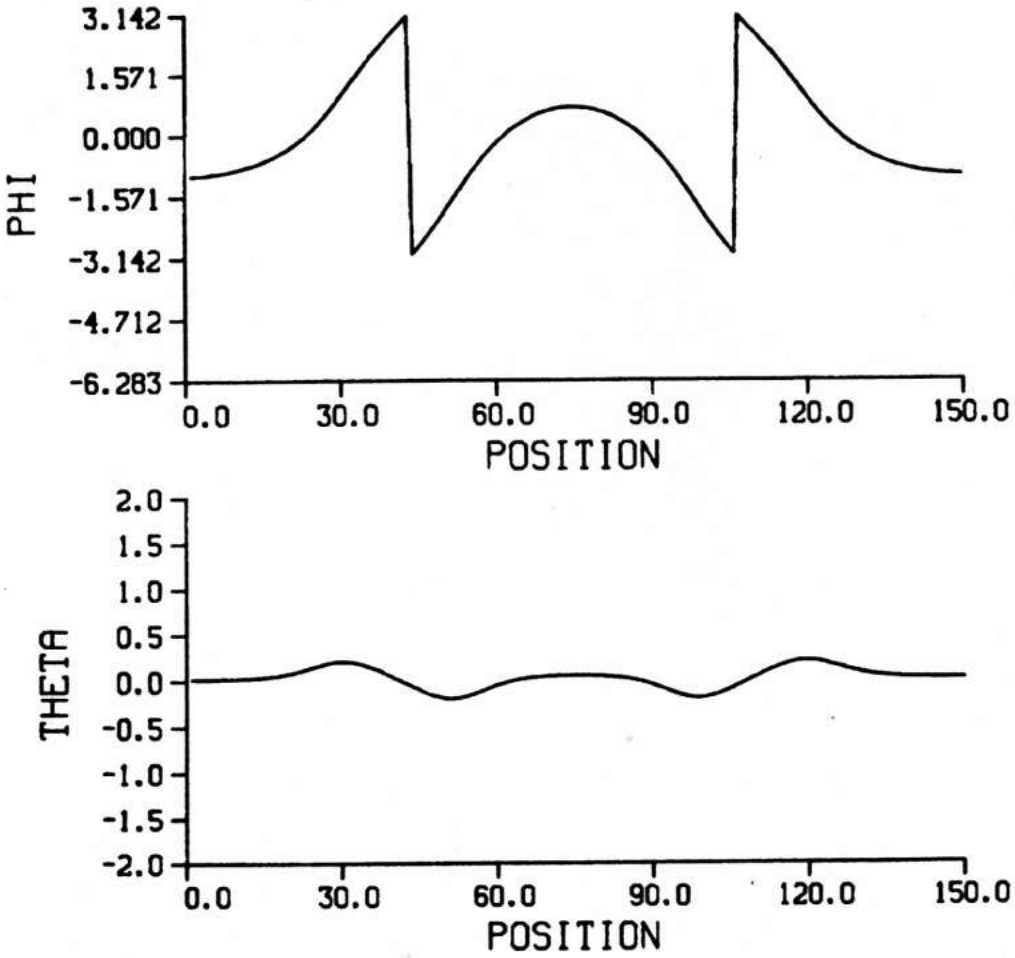

Figure 4.8a In-plane and out-of-plane angles ϕ and θ at t = 3000, for B_{ACX} = 4.0 kG, starting from the symmetric breather initial condition, Figure 4.7. The 2π discontinuities in ϕ are physically irrelevant.

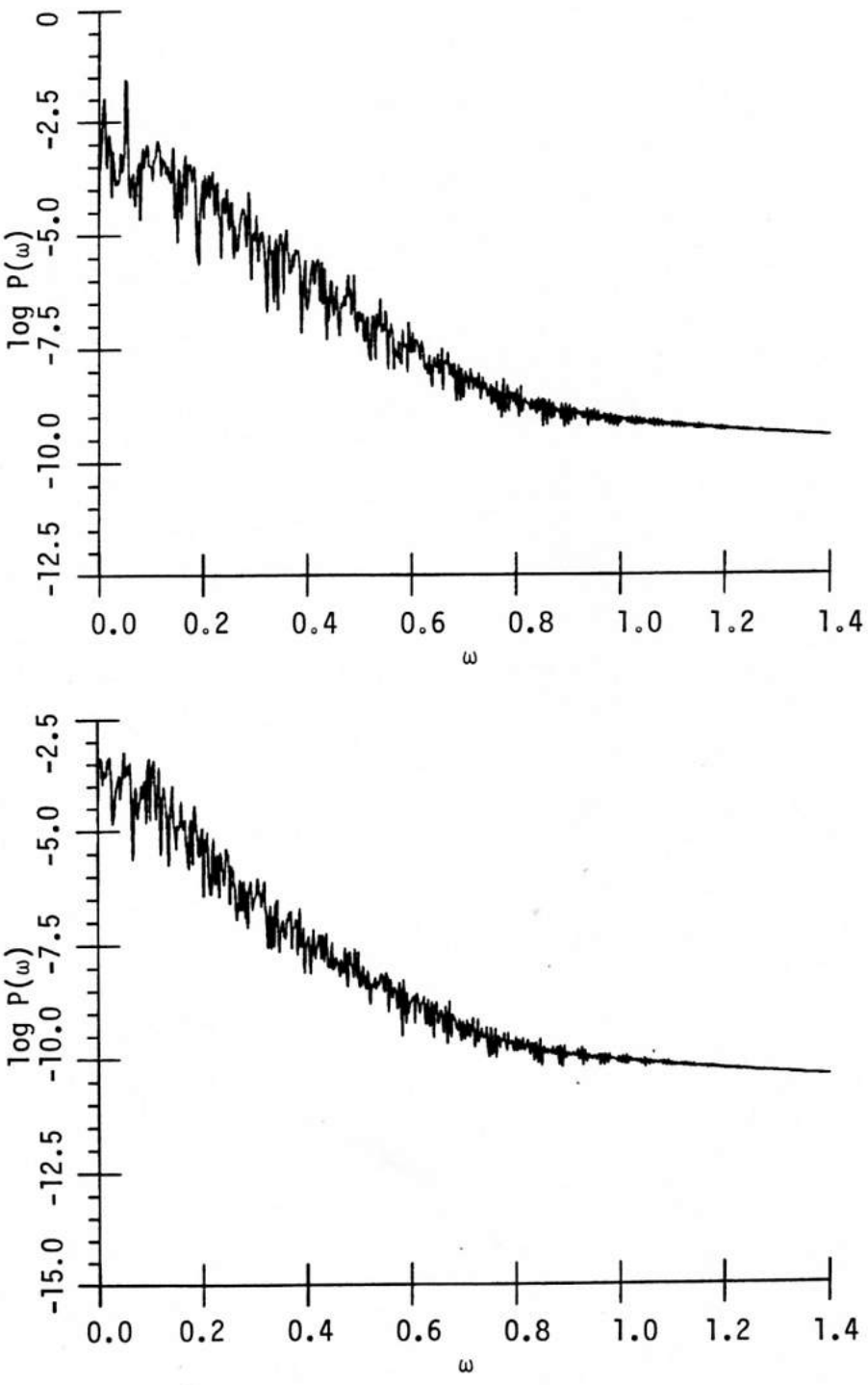

Figure 4.8b Power spectra (log scale) of the x(a) and z(b) components of the spin at the center of the chain, starting from symmetric breather initial conditions, with B_{ACX} = 4.0 kG. The driving frequency is ω = 0.05144 in these units.

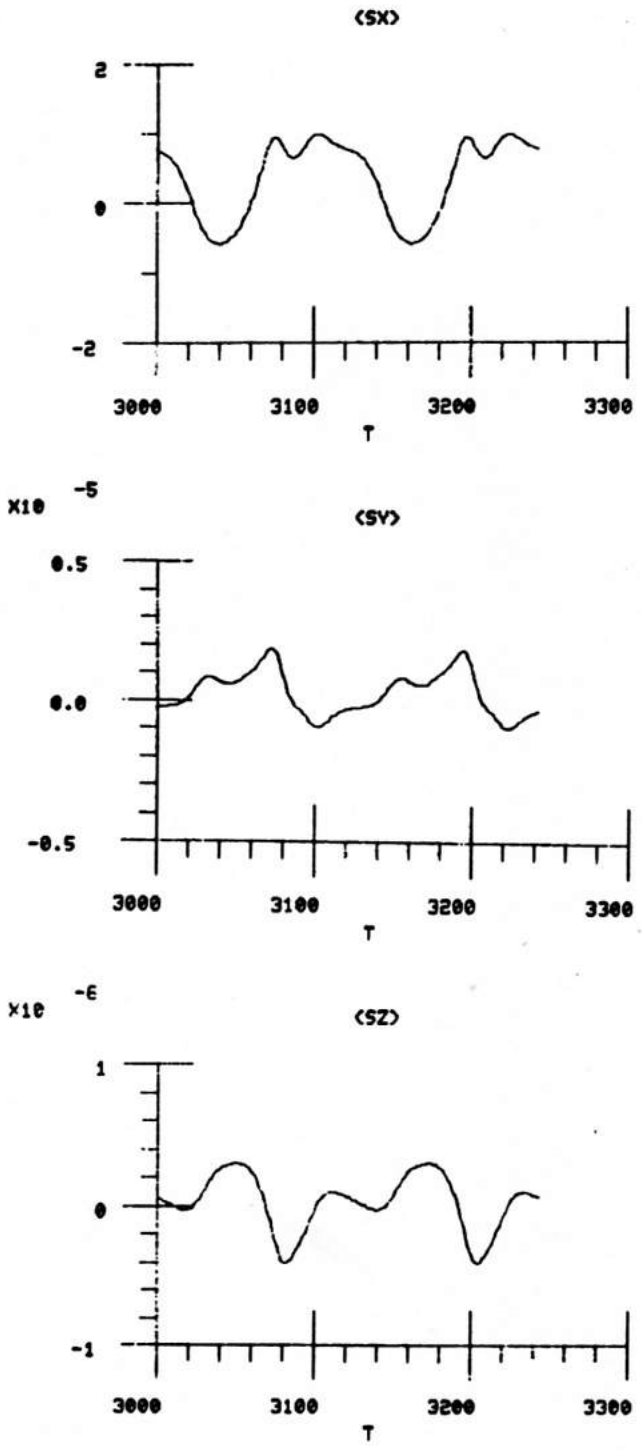

Figure 4.9a xyz components of $\langle\vec{S}(t)\rangle$ for B_{ACX} = 5.0 kG, starting from a random initial condition. The motion is synchronized with the driving frequency. The period of the driver is T = 122. Note the small size of the y and z components.

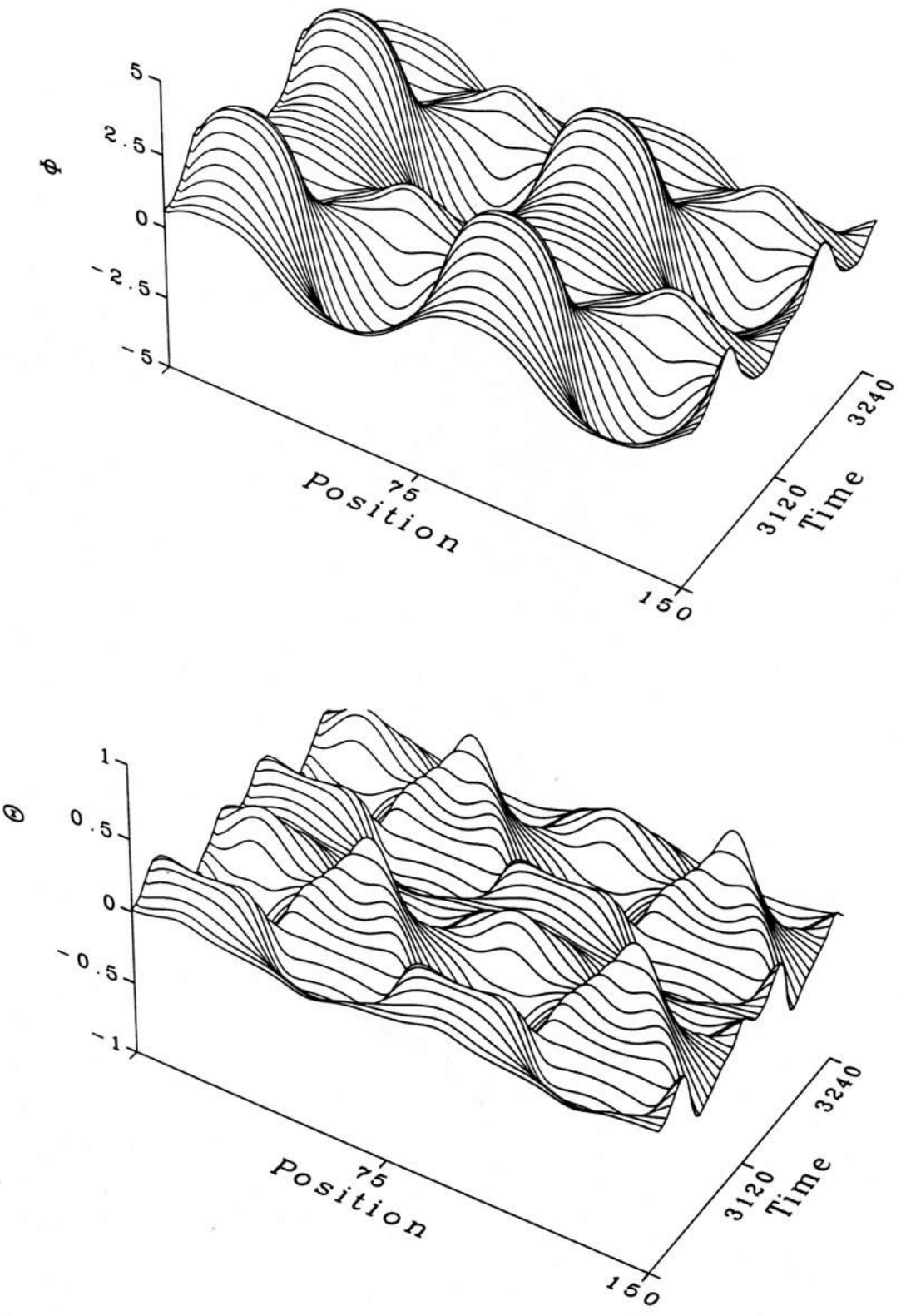

Figure 4.9b Space-time profiles for ϕ and θ, starting from a random initial condition at t = 0, with B_{ACX} = 5.0 kG. The solution is a standing wave.

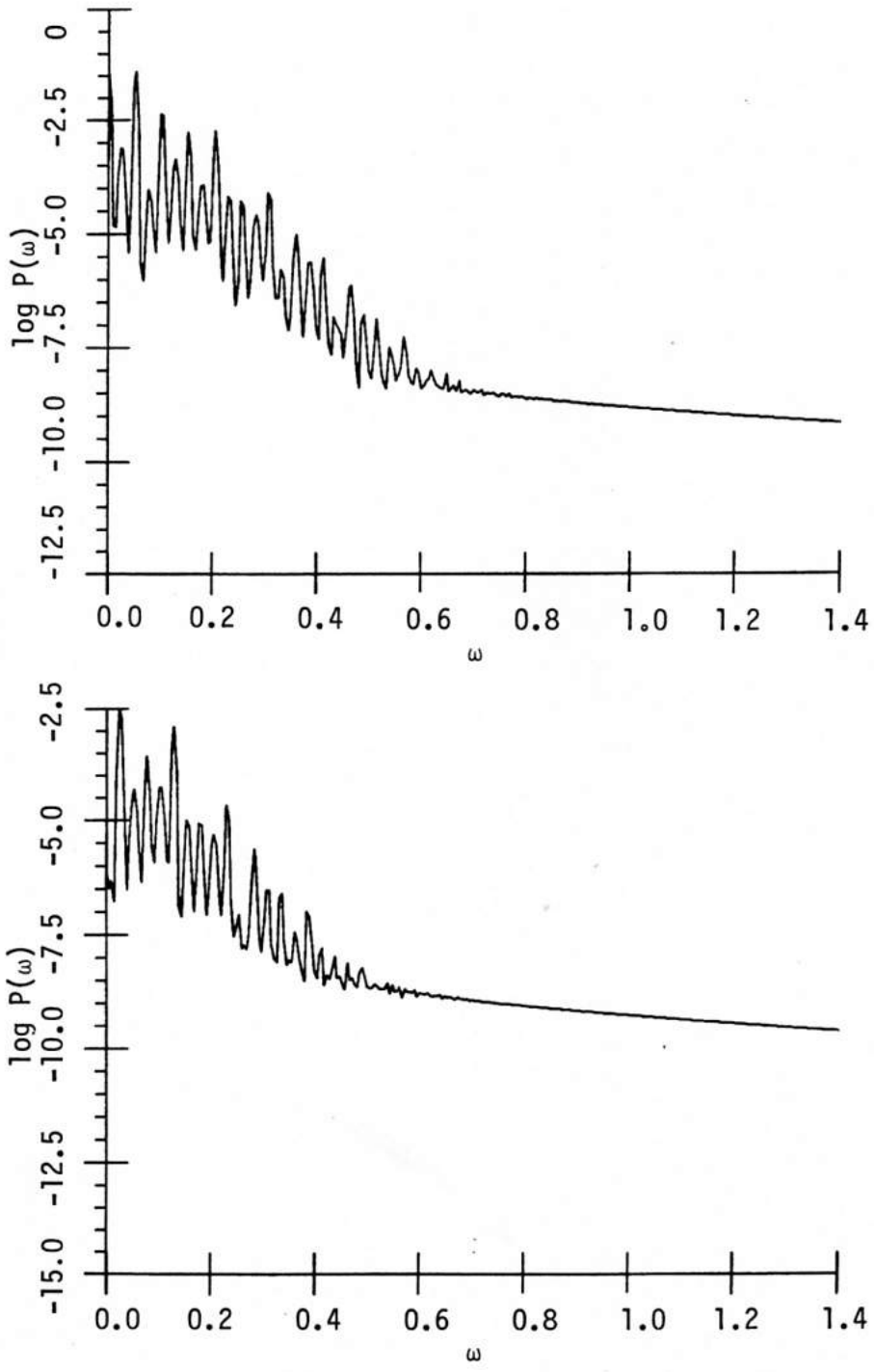

Figure 4.10a Power spectra (log scale) of the x(a) and z(b) components of the spin at the center of the chain, starting from symmetric breather initial conditions, with B_{ACX} = 5.0 kG. The lowest frequency peaks are at half the driver frequency.

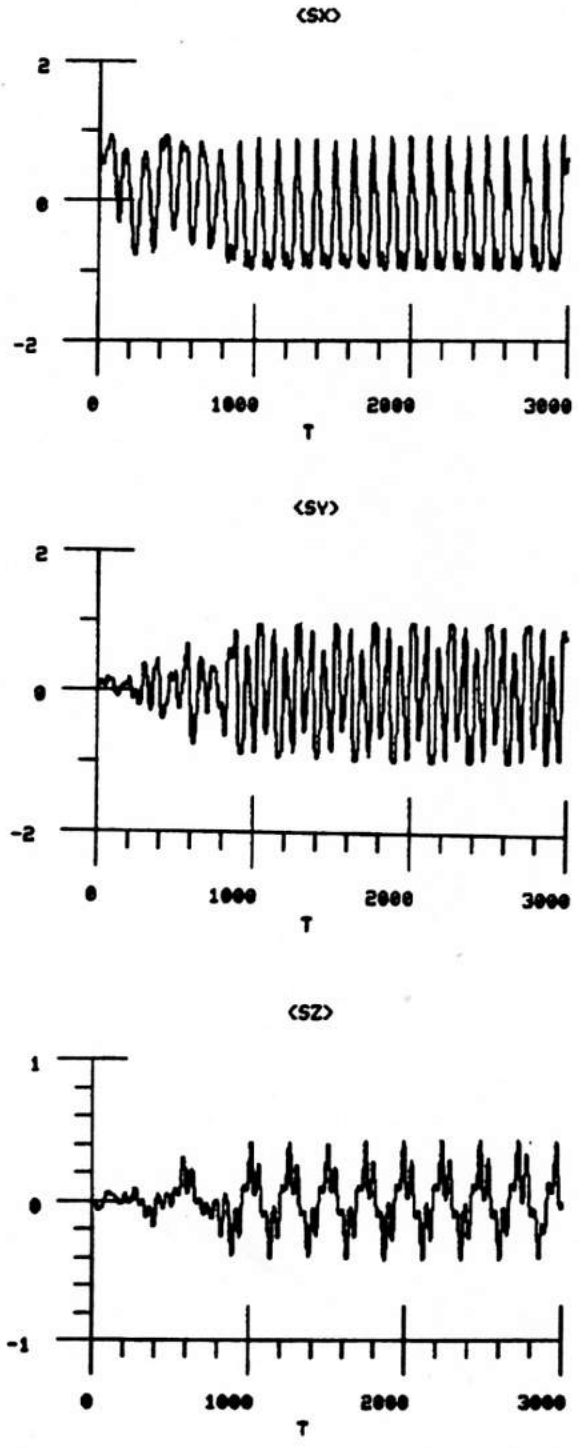

Figure 4.10b xyz components of $\langle \vec{S}(t) \rangle$ for B_{ACX} = 5.0 kG, starting from a symmetric breather initial condition. It is especially evident from the z-component that the period is twice the driver period, T = 122.

of the spin at the center of the chain. There is a scatter of data points which represents the initial transient, together with the stable long time orbit. The magnetization is shown in Figure 4.11b; in this case it represents the individual spin motions since they all move together. The y and z components move synchronized with the driving frequency, while the x-component moves at twice the driving frequency. This is made even more obvious in Figure 4.11c, where the power spectra of the x and z components are plotted.

Changing B_{ACZ} to 35.0 kG, and still using breather initial conditions, has a dramatic effect on both the space and time structure of the motion. The profile at t = 3000, shown in Figure 4.12a, is a pair of distorted breather-like structures. The magnetization, Figure 4.12b is now chaotic in time, although one may say that the z-component looks nearly periodic. But clearly the individual spin motion is chaotic, as seen in the phase plane and power spectrum for the z-component of the spin at the center of the chain, Figure 4.12c.

For this simulation, the GP dimension was calculated, for the individual spin components, using an embedding dimension of 8. In Figure 4.13, a typical graph of the correlation sum c(r) is shown, which is n(r) divided by the total number of possible pairs of data points (i,j). The graph was computed using x-components of the spins -- similar results of $\nu \sim 2$ are obtained for the y and z components. This is interpreted as indicating that there is only a small effective number of modes respondible for the chaotic dynamics, contrary to what might be expected for a set of noninteracting spins. The generation of coherent spatial structures is believed to be responsible for limiting the effective dimension of the dynamics.

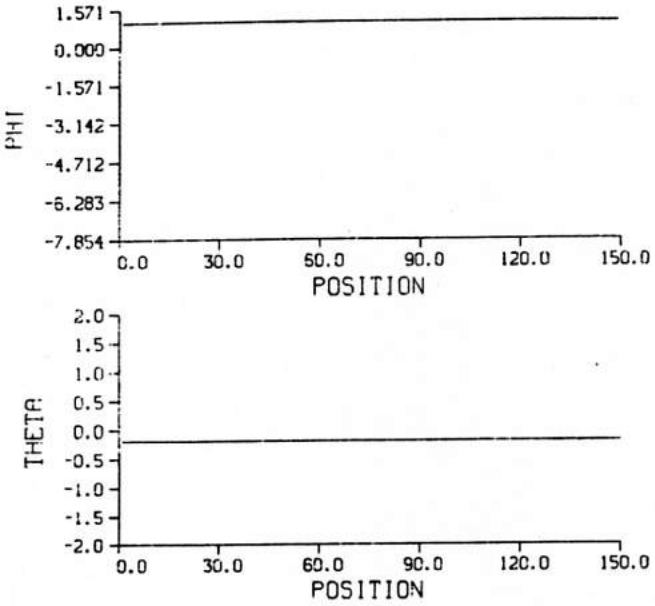

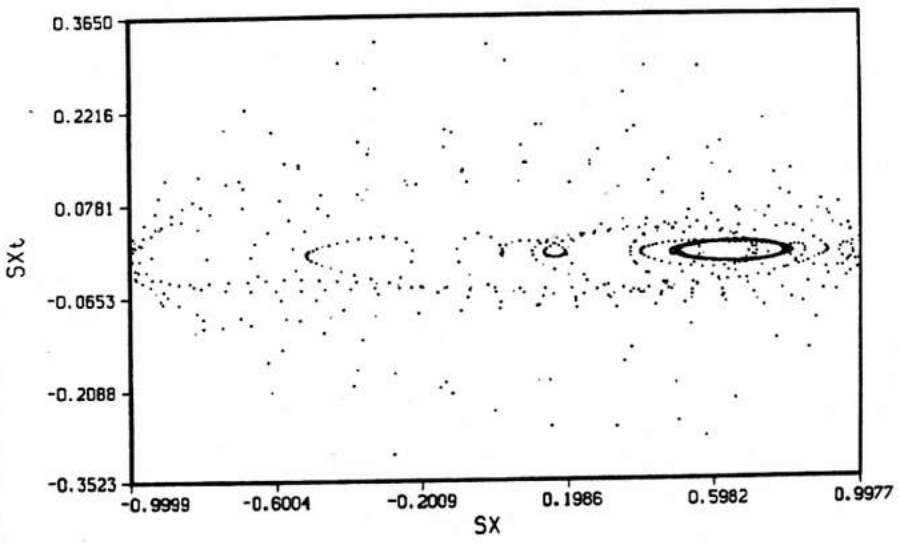

Figure 4.11a The flat profile for B_{DCX} = 5.0 kG, B_{ACZ} = 29.0 kG, using a breather initial condition, and the corresponding x phase plane for the center spin. All spins move together. The phase plane plot includes the initial transient.

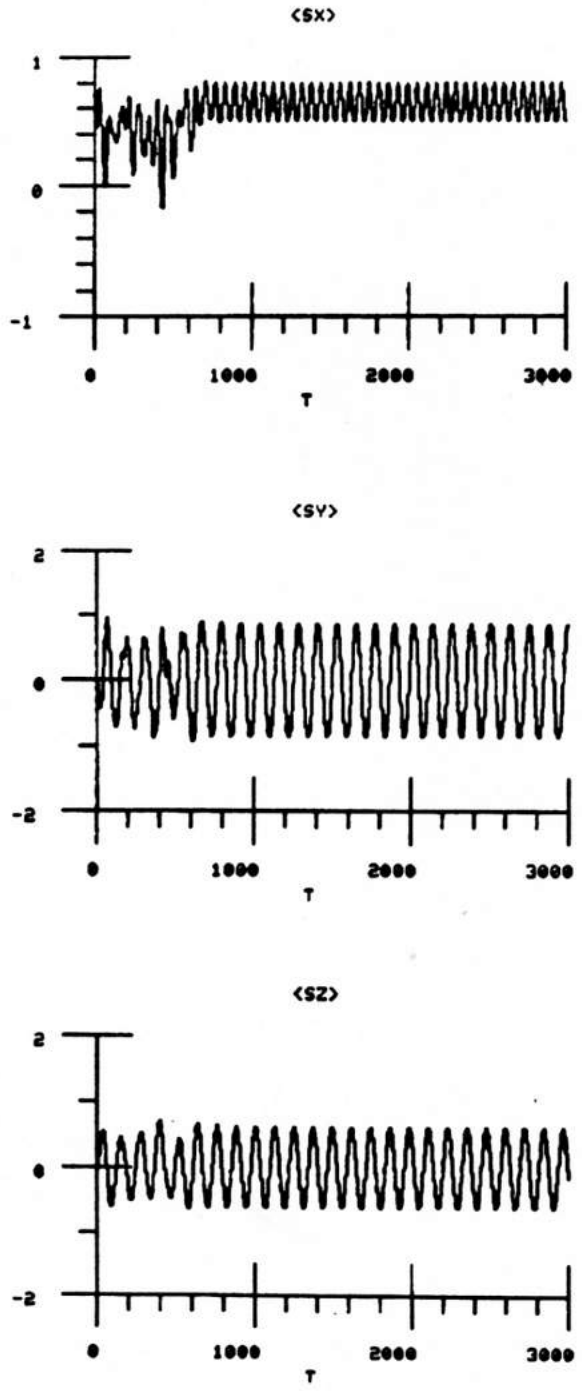

Figure 4.11b xyz components of $\langle \vec{S}(t) \rangle$ for B_{DCX} = 5.0 kG, B_{ACZ} = 29.0 kG, starting from a breather initial condition.

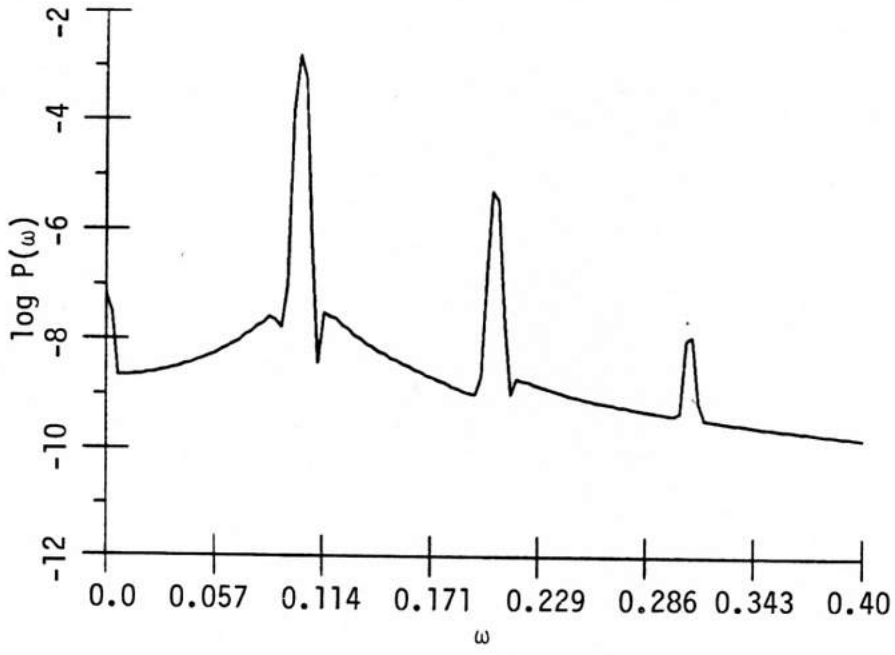

(a)

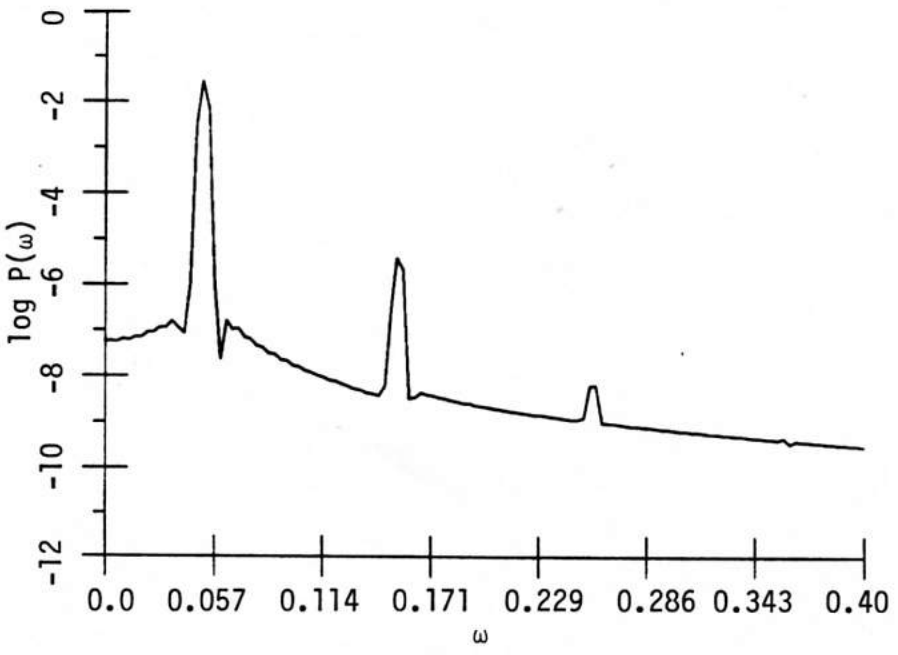

(b)

Figure 4.11c Power spectra of the x(a) and z(b) components for B_{DCX} = 5.0 kG, B_{ACZ} = 29.0 kG, starting from breather initial conditions.

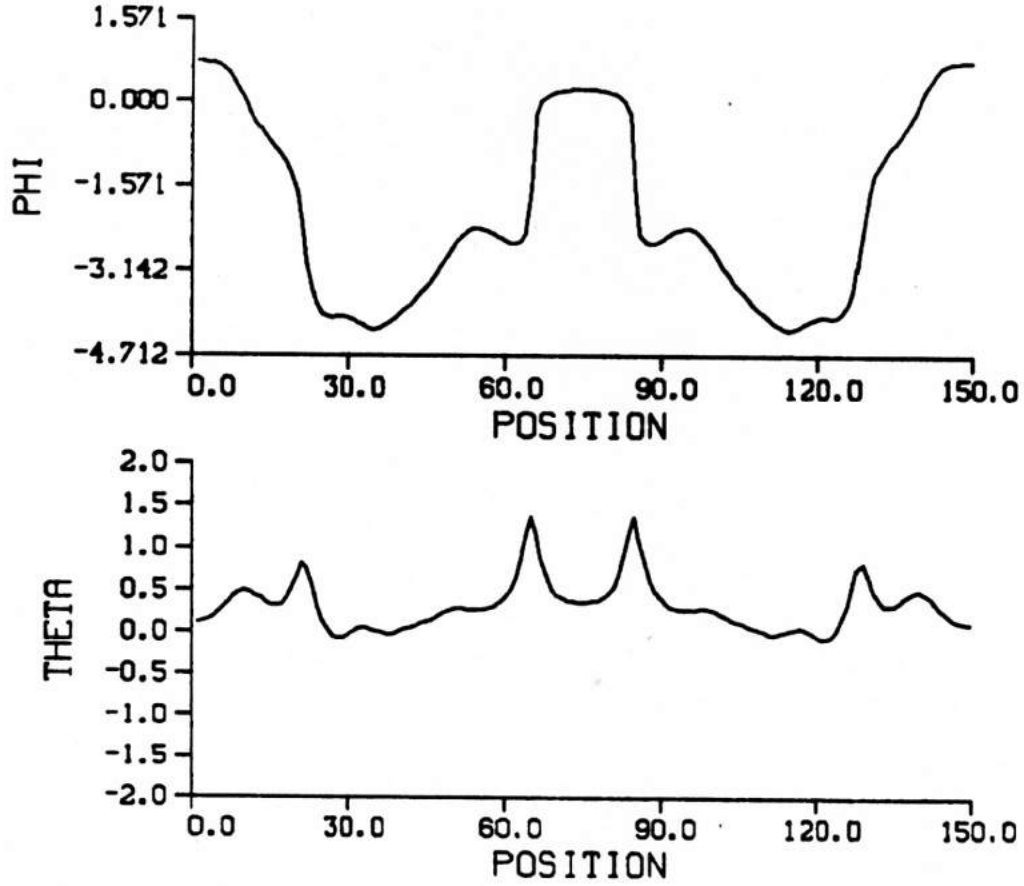

Figure 4.12a Spin profile at t = 3000, for B_{DCX} = 5.0 kG, B_{ACZ} = 35.0 kG, starting from a breather initial condition.

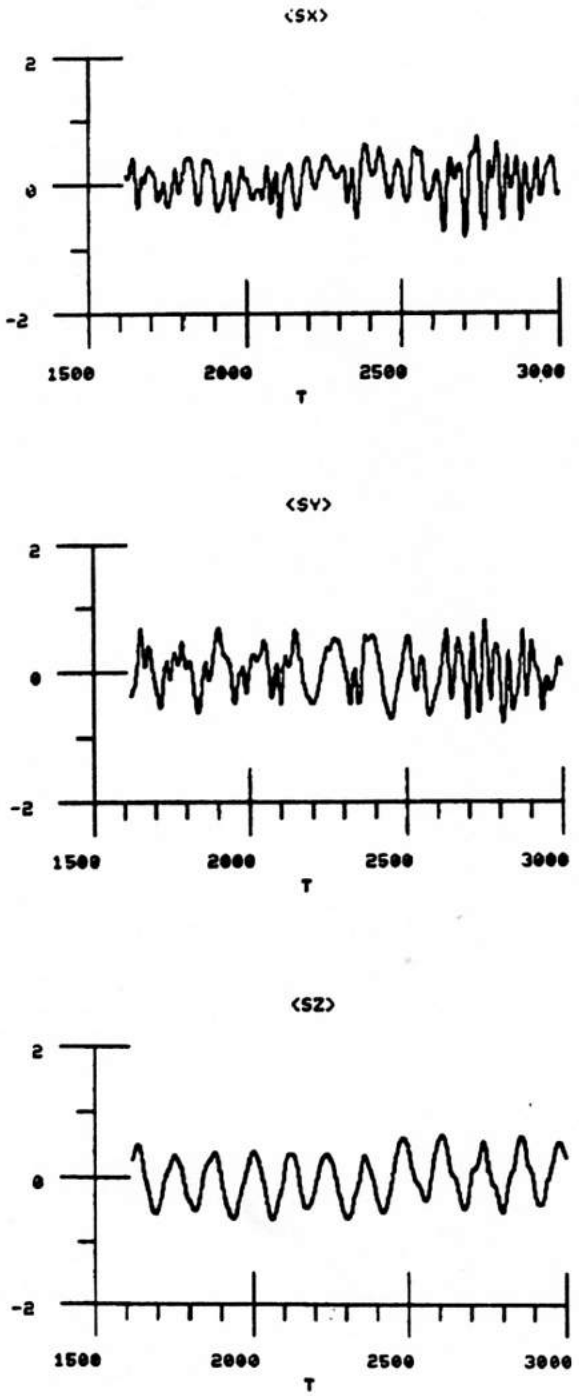

Figure 4.12b xyz components of $\langle \vec{S}(t) \rangle$ for B_{DCX} = 5.0 kG, B_{ACZ} = 35.0 kG, starting from breather initial conditions.

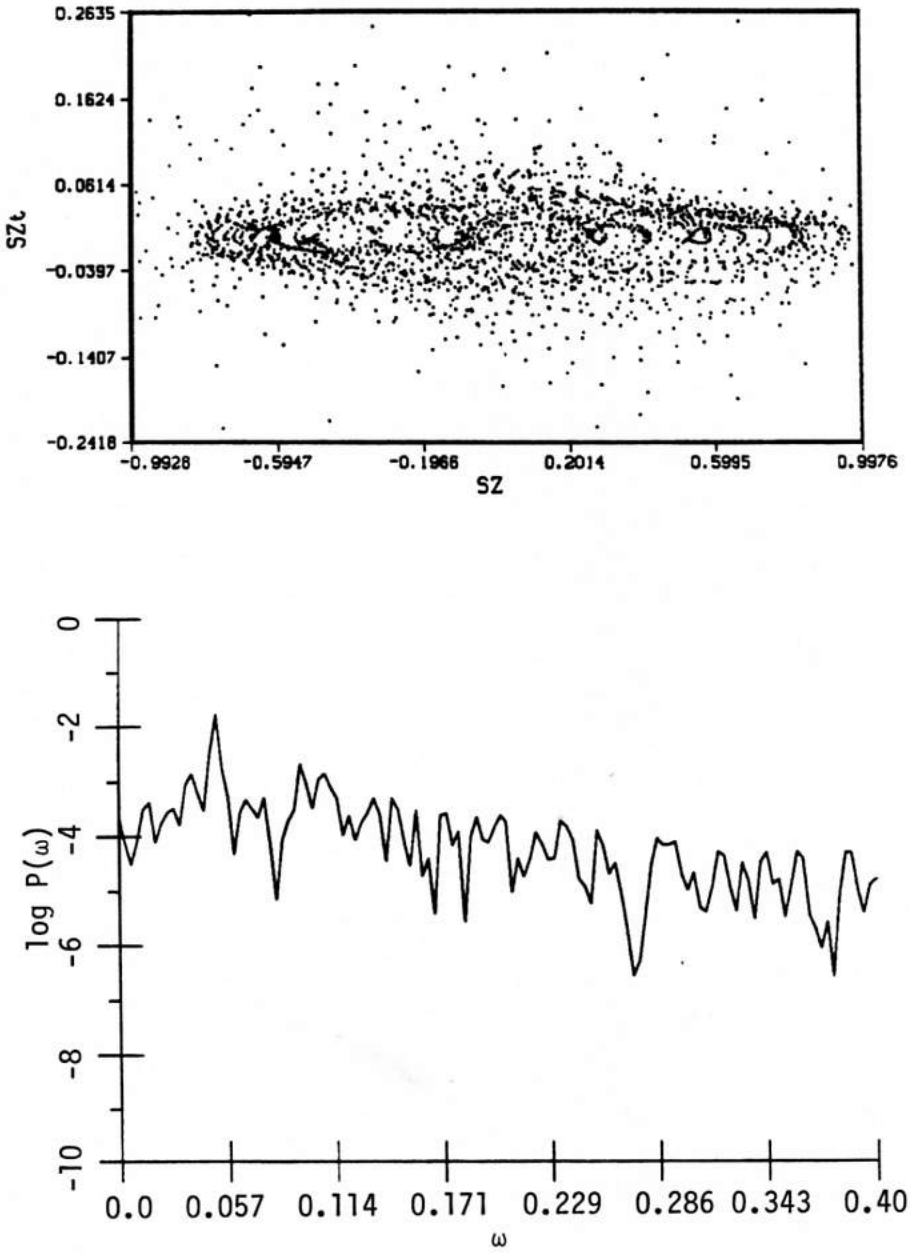

Figure 4.12c z-component phase plane and power spectrum for the spin at the center of the chain, using B_{DCX} = 5.0 kG, B_{ACZ} = 35.0 kG.

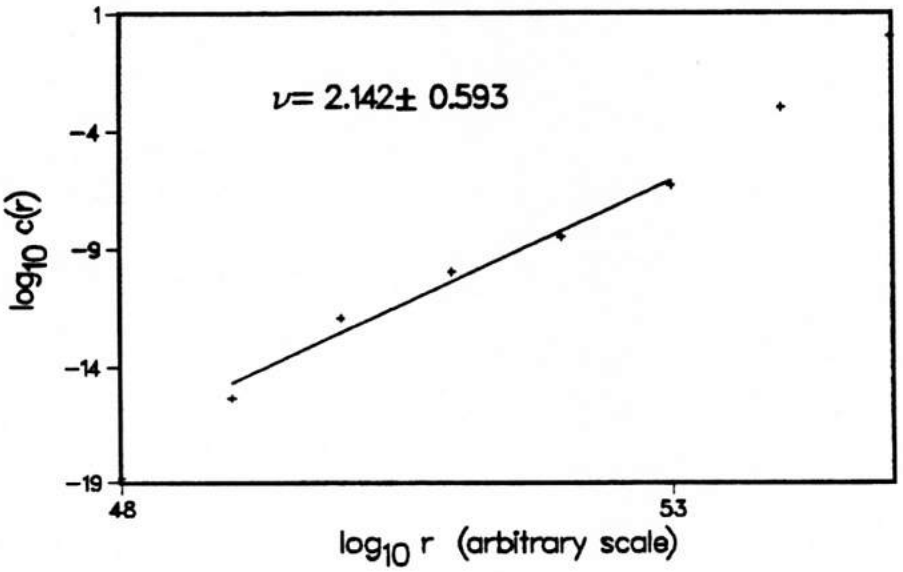

Figure 4.13 Log-log plot of the correlation sum c(r), which is directly proportional to n(r), equation (4-1), for B_{DCX} = 5.0 kG, B_{ACZ} = 35.0 kG, as obtained using x-components of 8 spin vectors on the lattice. Similarly, using the y and z components gives $\nu = 2.2 \pm 0.6$ and $\nu = 2.0 \pm 0.6$ respectively.

Example Three

The driving field configuration with parallel AC and DC fields in the easy plane was also found to have a chaotic window for B_{DCX} = 5.0 kG, B_{ACX} = 9.0 kG. For B_{ACX} slightly above or below 9.0 kG, the spatial structure was flat, starting from a random initial condition. Of course it is possible that some other slightly different initial conditions could produce a long lived coherent structure for these fields. A typical profile at B_{ACX} = 9.0 kG, with B_{DCX} = 5.0 kG, is shown in Figure 4.14. It appears to be a single kink in combination with other complicated structure. Note that for other random initial conditions we have obtained a single breather.

4.8 Summary

Through the use of numerical simulation of the equations of motion on a lattice, it has been demonstrated that it is possible to produce temporally chaotic spin motions in the easy-plane classical ferromagnet. For the field configurations tested, the chaos has been shown to be low-dimensional by numerical estimates of the Grassberger-Procaccia dimension. Typically the generation of long-lived spatial structures competes with the tendency for the spin motion to become chaotic, thereby restricting the effective dimensionality.

Three particular driving field configurations studied were most effective in producing chaos: 1) AC only in the easy plane; 2) parallel AC and DC in the easy plane, and 3) DC in the easy plane plus AC perpendicular to the easy plane, which reduces to a damped driven sG equation in the small out-of-plane angle limit. The field strengths used here for the $CsNiF_3$ anisotropy are experimentally accessible, but obtaining these strengths at the 25 GHz frequency may be too difficult,

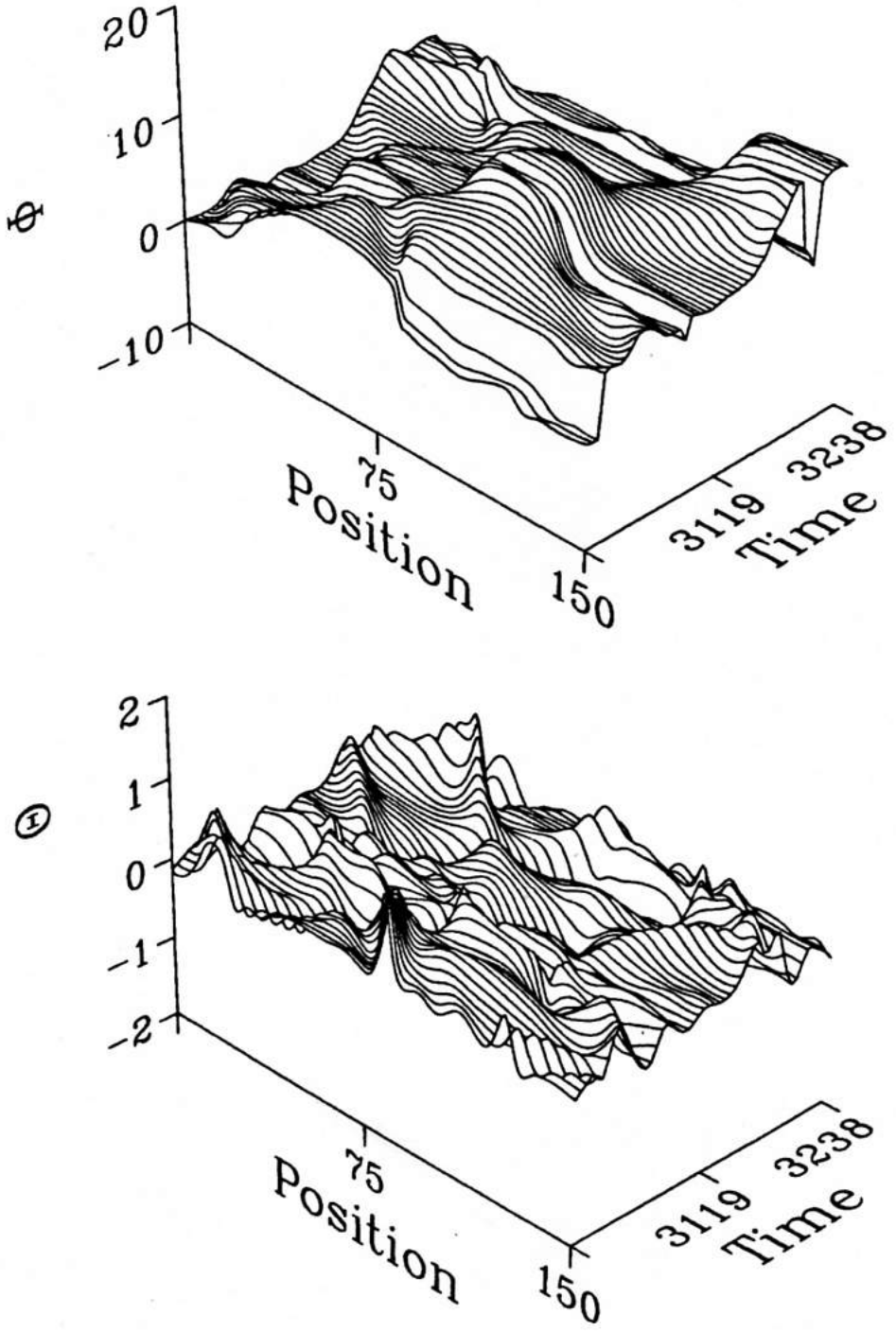

Figure 4.14 Space-time profile for B_{DCX} = 5.0 kG, B_{ACX} = 9.0 kG, starting from a random initial condition.

making it impossible to test these results for the real material. However, since 1-D magnets are so well characterized, they are excellent candidates for study in the emerging field of "solid state chaos" in real and accessible materials. (Other examples are Josephson lines and Josephson junctions, and charge density wave compounds.) Therefore, the possibility of other ways to produce space-time complexity in 1-D magnets should be pursued. Also, measurements of the magnetic susceptibility χ in these materials is becoming much more precise, and could serve as an important diagnostic for learning about the dynamics of the nonlinear excitations.